JGR Atmospheres

RESEARCH ARTICLE
10.1029/2022JD038101

Cold-Season Surface Energy Balance on East Rongbuk Glacier, Northern Slope of Mt. Qomolangma (Everest)

Weigang Liu[1,2], Xingguo Yang[3], Michiel R. van den Broeke[4], Baojuan Huai[4,5], Diyi Yang[2,6], Dongqi Zhang[2], Xiang Qin[7], Ping Yue[1], Heling Wang[1], and Minghu Ding[2,7]

[1]Key Laboratory of Arid Climatic Change and Reducing Disaster of Gansu Province, Key Open Laboratory of Arid Climate Change and Disaster Reduction of CMA, Institute of Arid Meteorology, China Meteorological Administration, Lanzhou, China, [2]State Key Laboratory of Severe Weather, Chinese Academy of Meteorological Sciences, Beijing, China, [3]Gansu Meteorological Bureau, Lanzhou, China, [4]Institute for Marine and Atmospheric Research, Utrecht University, Utrecht, The Netherlands, [5]College of Geography and Environment, Shandong Normal University, Jinan, China, [6]Haining Meteorological Bureau, Haining, China, [7]State Key Laboratory of Cryospheric Science, Northwest Institute of Eco-Environment and Resources, Chinese Academy of Sciences, Lanzhou, China

Key Points:

- We present 3.5 months of autumn and wintertime glacier surface energy balance at 6,523 m above sea level on Mt. Qomolangma
- There was a semi-permanent surface radiative loss due to deficient clouds, large solar zenith angle, and high albedo of glacier surface
- Clouds reduced solar irradiance more than increased longwave radiation, implying that their shading effect surpassed the greenhouse effect

Correspondence to:
M. Ding,
dingminghu@foxmail.com

Citation:
Liu, W., Yang, X., van den Broeke, M. R., Huai, B., Yang, D., Zhang, D., et al. (2023). Cold-season surface energy balance on East Rongbuk glacier, northern slope of Mt. Qomolangma (Everest). *Journal of Geophysical Research: Atmospheres*, *128*, e2022JD038101. https://doi.org/10.1029/2022JD038101

Received 9 NOV 2022
Accepted 28 FEB 2023

Abstract As the highest peak on the earth, Mt. Qomolangma provides an unparalleled platform to study glacier-atmosphere interaction. Although glacier surface energy balance (SEB) on Mt. Qomolangma was examined during warm season, relevant knowledge during cold season is still unknown, which prevents a complete understanding of all-season glacier SEB on it. Based on an in-situ observation from October 2007 to January 2008, this study presents a cold-season glacier SEB result at 6,523 m above sea level on Mt. Qomolangma and identifies its atmospheric control. Our results show that the observational period experienced strong winds and deficient clouds. Near-surface wind speeds usually exceeded 10 m s^{-1}, resulting in a substantial sensible heat transport toward glacier and thus enhancing outgoing longwave radiation, which, under the combined effect of deficient clouds, eventually caused an increase in longwave radiative loss. The large solar zenith angle and relatively high albedo of the glacier surface led to a small absorption of solar irradiance, which, in combination with the strong longwave radiation loss, resulted in a semi-permanent surface radiative loss. Uncommon over the highly reflective glacier surface, clouds decreased the incident solar radiation more than increased the longwave radiation, demonstrating that the clouds' shading effect surpassed its greenhouse effect. As a vital heat sink, the turbulent latent heat induced an average sublimation rate of 0.8 mm water equivalent per day. This study provides valuable insights into the atmospheric control on the cold-season glacier-atmosphere interaction at high altitudes on Mt. Qomolangma when meteorological variables are subject to the westerlies.

Plain Language Summary Mt. Qomolangma is the highest mountain on the earth. Qomolangma's glacier retreat is a warning sign for rapid climate warming. Understanding the atmospheric control on Qomolangma's glacier mass loss is critical. This paper thoroughly examines how the energy associated with Qomolangma's glacier mass loss at 6523 m above sea level was governed in the cold season. We find that wind speed is an important factor. On one hand, its increase enhanced the energy input toward glacier, increasing surface temperature and thus letting more energy escape from glacier surface under the combined influence of small cloud cover; on the other hand, the increase in wind speed enhanced the mass loss of sublimation, lowering surface temperature. Cloud cover is another factor. The clouds' shading effect of decreasing incoming sunlight surpassed its greenhouse effect of increasing energy toward glacier, making less energy arriving at the glacier surface and thus decreasing mass loss. Additionally, at the highly reflective glacier surface, glacier received weak sunlight in cold season because a significant portion of the relatively modest incoming sunlight was reflected to the sky. These results provide valuable insights into the atmospheric control on Qomolangma's glacier mass loss in the cold season.

1. Introduction

The Tibetan Plateau (TP) and its surroundings have the highest and largest mountain mass in the world (Duan & Wu, 2006), earning them the name of "the third pole" (Kang et al., 2022; Qiu, 2008). The mountains cover an east-west distance of over 2000 km and a north-south distance of over 1000 km (Benn & Owen, 1998), holding the third largest ice mass in the world (Meng et al., 2019; Xu et al., 2009) with a total glacial area of

~100,000 km^2 (Kotlyakov et al., 2012; Yao et al., 2012). Being a large natural solid water reservoir and the source of several prominent Asian rivers, glaciers on TP contribute substantially to drinking water, irrigation for agriculture, and hydropower supply (Scherler et al., 2011) for about 800 million people downstream (Pritchard, 2019). As natural buffers of hydrological seasonality (Bolch et al., 2012), glaciers can significantly modify regional hydrology (Kaser et al., 2010).

Given the significance of the TP's glaciers for the regional environment, efforts to monitor their change have increased over the past decades (Barandun et al., 2021; Bhattacharya et al., 2021). These studies show that TP's glaciers have experienced persistently increasing but spatially heterogeneous mass loss since the 1960s (Yao et al., 2012), with the highest mass wastage in the southeastern region of TP (Nyaingentanglha) and greatest mass gain in Kun Lun (Hugonnet et al., 2021; Jouberton et al., 2022; Shean et al., 2020).

Glaciers are sensitive to climate change (Liang et al., 2019, 2020; Scherler et al., 2011). To better understand the heterogeneous response of TP's glacier to climate change, glacier surface energy balance (SEB) must be well understood since it is an effective means to physically describe the relationship between the glacier and the overlying atmosphere (W. Yang et al., 2013). Previous glacier SEB studies (Fugger et al., 2021; G. Zhang et al., 2013; S. Li et al., 2018; Sun et al., 2018; W. Yang et al., 2011, 2017; Zhu et al., 2015, 2018) have described a general SEB pattern in the debris-free surfaces of TP's glaciers: energy sink is mainly composed of net longwave radiation, latent heat, and melting energy, while the energy source primarily constitutes net shortwave radiation and sensible heat, with an exception that, for the debris-covered glacier surfaces, the sensible heat generally represents energy sink (Fugger et al., 2022; W. Yang et al., 2017) because of the higher temperatures of the debris surface than those in the overlying near-surface atmosphere. Recent studies in the Langtang valley of Nepal highlighted the importance of turbulent latent heat (Stigter et al., 2018) and meltwater refreezing-released heat (Stigter et al., 2021; Veldhuijsen et al., 2021) in the snow-atmosphere interaction. A more recent study by Mandal et al. (2022) summarized almost all of the glacier SEB researches carried out on TP in the cold season and emphasized the importance of clouds and winds in surface sublimation. Despite the above advances in the glacier SEB studies, most of these investigations were carried out at elevations lower than 6000 m above sea level (asl). Glacier SEB knowledge at altitudes >6000 m asl is still scarce.

As the highest mountain on the earth, Mt. Qomolangma (Everest) is a unique site suitable for carrying out high-altitude glacier SEB research. During the premonsoon climbing season of 2019, a meteorological observation network was set up on the southern slope of Mt. Qomolangma (Matthews et al., 2020; Potocki et al., 2022), with three automatic weather stations (AWSs) located at elevations of 6464 m asl, 7945 m asl, and 8430 m asl, respectively. Based on a 6-month observation of this network, the glacier SEB was analyzed at 7945 m asl and 8430 m asl, respectively, emphasizing that melting is possible at the two observational sites or even at the mountain summit (approximately 8848 m asl) during the warm premonsoon season despite the persistently below-freezing air temperatures. However, the above glacier SEB result was obtained with an assumed constant snow albedo (0.8) rather than the albedo of the "true" glacier surface, which may result in unreliable SEB results. Using meteorological data in-situ measured from 5207 m to 7028 m asl on the northern slope of Mt. Qomolangma, X. Yang et al. (2015, 2018) analyzed the spatiotemporal variability in the near-surface meteorological variables from May 2007 to September 2008. The detailed glacier SEB, however, was not examined. From May to July 2005, a warm-season glacier SEB experiment was conducted at 6523 m asl on the East Rongbuk glacier, northern slope of Mt. Qomolangma. This study highlighted the importance of clouds in the glacier-atmosphere interaction during the monsoon period (W. Liu et al., 2021). The atmospheric control on the glacier SEB pattern during the westerlies-controlled cold season, however, is unclear. This inhibits an all-season understanding of the glacier-atmosphere interaction on Mt. Qomolangma. To close this knowledge gap, a new AWS was installed at the same observational site as in 2005 on the East Rongbuk glacier in October 2007. Based on the 3.5 months of meteorological observation, this paper investigates the glacier SEB pattern at the 6,253 m asl in the cold season, aiming to provide valuable insights into the westerlies-controlled glacier-atmosphere interaction at high altitudes on Mt. Qomolangma.

The remainder of this paper is organized as follows: Section 2 describes the study region and measurement program, followed by Section 3 introducing methodology and Section 4 displaying the glacier SEB result; discussion is presented in Section 5, and conclusions are shown in Section 6.

2. Study Region and Measurement Program

The East Rongbuk glacier (Figure 1), located on the northern slope of Mt. Qomolangma, is a tributary of the Rongbuk glacier (W. Liu et al., 2010). According to the second glacier inventory of China released in 2012 (Guo

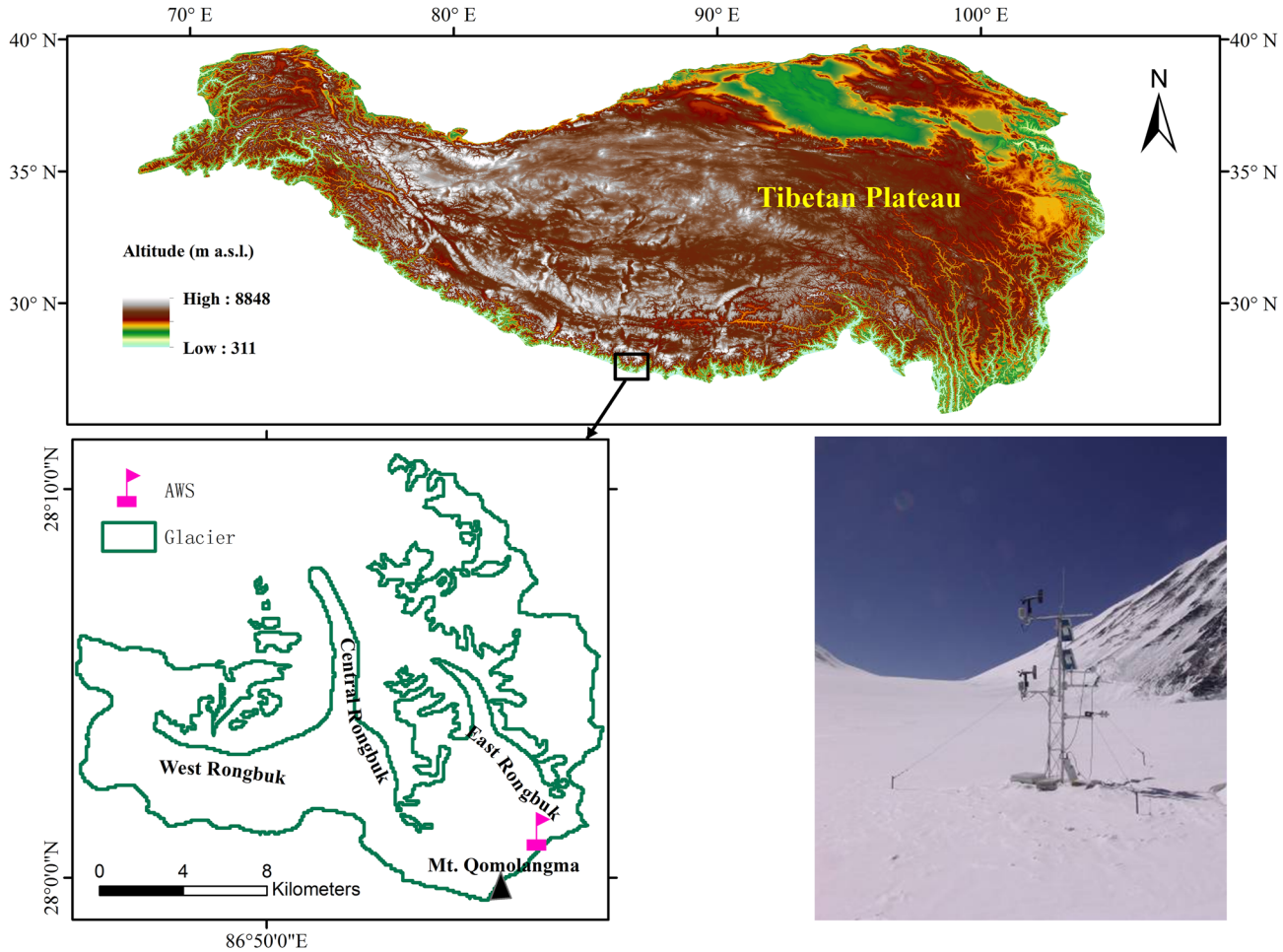

Figure 1. Locations of the East Rongbuk glacier and our AWS site.

et al., 2015; S. Liu et al., 2012), it spans elevations from 5607 m to 7551 m asl, with an area of 41.7 km^2 and a volume of 4.6 km^3. Its equilibrium line altitude was estimated at 6217 m asl in 1994 (Mi & Xie, 2002). From 1974 to 2006, the East Rongbuk glacier experienced pronounced elevation and glacier mass decreases, with their change rates at -0.28 ± 0.23 m a^{-1} and -0.24 ± 0.27 m a^{-1} water equivalent, respectively (Ye et al., 2015). Due to significant climatic warming (Pang et al., 2020; Ren et al., 2004; X. Yang et al., 2018), its terminus retreated at an average rate of ~5.5 m a^{-1} over 1996–2001 (Ren et al., 2004).

The local climate is under the combined control of the south Asian summer monsoon (Zhou et al., 2008; Zou et al., 2008, 2009) and the westerlies (Yao et al., 2012). From late spring (typically from mid-June (Chang & Chen, 1995)) to autumn every year, the south Asian summer monsoon prevails over the Indian subcontinent, with moist air transported from the Bay of Bengali (Webster & Yang, 2010) and thus leading to a wet season. From late autumn to early spring next year, however, the south Asian summer monsoon withdraws and the local climate is affected by the southern branch of the westerlies (B. Wang, 2006), resulting in a dry environment.

On 3 October 2007, an AWS was erected on the Ruopula Col (6523 m asl, 28°1'N, 86°57'E, Figure 1) in the accumulation zone of the East Rongbuk glacier. Using a steel tripod, it was placed on a relatively flat surface, with wooden blocks placed under each leg for stability and preventing it from melting into the firn. Table 1 lists details of the AWS instrumentation. Air temperature, relative humidity (RH), and wind speed/direction were measured at two levels, with the initial mounting heights at 2.0 and 4.0 m, respectively. The AWS was inspected and maintained for horizontal aligning and preventing rime deposition approximately once per 30 days. The four-radiation components were measured at the height of 1.5 m, with a reported measurement accuracy of less than ±5% (van den Broeke, van As, Reijmer, & van de Wal, 2004) for the shortwave radiation measurement and

Table 1
Technical Specifications of the AWS's Sensors and Installation Heights

Elements	Sensor type	Accuracy (calibration range)	Installation height (in m)
Air temperature (°C)	Vaisala HMP 45D	±0.2°C (−40°C–60°C)	2.0, 4.0
Relative humidity (%)	Vaisala HMP 45D	±2% (0.8%–100%)	2.0, 4.0
Wind speed (m s^{-1})	Young 05103	±0.3 m s^{-1} (0–100 m s^{-1})	2.0, 4.0
Wind direction (°)	Young 05103	±3° (0–355°)	2.0, 4.0
Air pressure (hPa)	PTB210	±0.35 Pa (50–1100 hPa)	0.5
Incident solar radiation (W m^{-2})	K&Z CNR1	±10% for daily totals	1.5
Reflected shortwave radiation (W m^{-2})	K&Z CNR1	±10% for daily totals	1.5
Incoming longwave radiation (W m^{-2})	K&Z CNR1	±10% for daily totals	1.5
Outgoing longwave radiation (W m^{-2})	K&Z CNR1	±10% for daily totals	1.5

up to a total daily net radiation uncertainty of 10 W m^{-2} (Michel et al., 2008). Continuous meteorological data were recorded from 3 October 2007 to 18 January 2008, during which all sensors worked well and the data integrity was excellent. All variables were sampled at 1-min intervals, after which ten-min averages were stored in a Campbell CR1000 data logger. These data were assembled into hourly means for glacier SEB calculations in this study. There was no snow surface height measurement, that is, meteorological variables were not corrected for height change. Visual observations confirmed that the sensor height remained within only 15 cm of the installation height over the observational period.

Precipitation data were unavailable because no precipitation was measured at our AWS and nearby. Nevertheless, the possible snowfall episodes can be identified by the increase in the surface albedo measured by the AWS. According to the "accumulated" albedo introduced in the following Section 4.2.1, it is approximated that snowfall episode likely lasted 15 days out of the whole 108-day observation, equivalent to a precipitation frequency of 14%. In contrast, liquid precipitation was not possible at this high altitude of 6523 m asl because of the substantially low air temperatures (Section 4.1). The AWS is just located on the Ruopula Col, a typical notch on Mt. Qomolangma through which the wintertime westerly flow can easily intrude into the northwest-oriented East Rongbuk valley, thus producing strong winds with directions nearly constant in cold season. Beijing time, which is 2 hr earlier than the local time, was utilized throughout our observation. In addition, the reanalysis data from the fifth generation ECMWF reanalysis for the global climate and weather (ERA5) at the 450-hPa level (geopotential height field, wind and air temperature fields) were used for synoptic analysis.

3. Methods

3.1. Model Description

The glacier SEB model used in this study is very similar to that previously utilized by van den Broeke, Reijmer, and van de Wal (2004), van den Broeke, Smeets, Ettema, Munneke, et al. (2008), van den Broeke, Smeets, Ettema, van der Veen, et al. (2008), and Kuipers Munneke et al. (2009, 2012). The model performs well under conditions of low incident solar radiation in polar regions, which is quite similar to the radiative conditions of this study. Additionally, this model can be conveniently evaluated using the "measured" surface temperature derived from the surface-emitted longwave radiation. Using hourly AWS data as input, the model solves for the hourly surface temperature T_s for which the glacier SEB is closed:

$$\mathrm{SR}\downarrow + \mathrm{SR}\uparrow + \mathrm{LR}\downarrow + \mathrm{LR}\uparrow + \mathrm{SH} + \mathrm{LE} + \mathrm{G} + \mathrm{QP} + \mathrm{QM} = 0. \quad (1)$$

All components are in W m^{-2} and are defined as positive when directed toward the glacier surface (Oke, 1987). Equation (1) assumes that all energy is absorbed or emitted at the glacier surface. QM, a residual term of Equation (1), represents the melting energy; SR↓ and SR↑ are the incoming and reflected shortwave radiations directly measured by the AWS. LR↓ is the incoming longwave radiation measured by the AWS. LR↑ is the outgoing longwave radiation calculated by the Stefan-Boltzmann equation using T_s (LR↑ = 0.97 σ T_s^4, 0.97 is the surface emissivity (Kondo & Yamazawa, 1986) and $\sigma = 5.67 \times 10^{-8}$ W m^{-2} K^{-4}). SH is the turbulent sensible heat, and

LE is the turbulent latent heat. G represents the subsurface heat and is estimated using the vertical temperature distribution in the near-surface snow layers based on the SOMARS model (Greuell & Konzelmann, 1994), with a skin layer formulation where penetration of shortwave radiation is neglected (van den Broeke et al., 2011). QP represents the heat flux supplied by liquid precipitation since rainfall can add energy to the glacier surface (D. Yang et al., 2021). However, given the low air temperature observed by the AWS (see Section 4.1), rainfall was impossible at our observational site. Therefore, QP is neglected in this study.

The pyranometer (K&Z CM3) for SR↓ measurement has a poor cosine response at low sun angles (van den Broeke, van As, Reijmer, & van de Wal, 2004), which may result in errors in net radiation (SRnet) calculation (SRnet = SR↓ + SR↑) when raw, hourly albedo values are used directly. To eliminate these errors, van den Broeke, van As, Reijmer, and van de Wal (2004) proposed a wildly-used method to accurately calculate SRnet. This method is based on the fact that SR↑ is diffuse and is therefore less sensitive to measurement errors in SR↓. It is expressed as:

$$\mathrm{SRnet} = -\mathrm{SR}\uparrow(1-\alpha)/\alpha \approx -\mathrm{SR}\uparrow(1-\alpha_{\mathrm{acc}})/\alpha_{\mathrm{acc}}, \tag{2}$$

$$\alpha_{\mathrm{acc}} = \sum_{0}^{24\mathrm{h}} |\mathrm{SR}\uparrow| / \sum_{0}^{24\mathrm{h}} |\mathrm{SR}\downarrow|, \tag{3}$$

where α is surface albedo, α_{acc} is the "accumulated" surface albedo, that is, the ratio of cumulative |SR↑| and |SR↓| over a time window of 24 hr centered around the observation time. In addition, the observed nighttime SR↓ and SR↑ values were occasionally non-zero. In such cases, they were set to null.

SH, LE, G, and LR↑ on the left-hand side of Equation (1) are more or less directly functions of T_s (Kuipers Munneke et al., 2012), which can be calculated using an iterative way for which all terms in Equation (1) can be added up to zero (Kuipers Munneke et al., 2012). The initial T_s was derived by rearranging Stefan-Boltzmann equation $\mathrm{LR}\uparrow = 0.97\,\sigma\,T_s^4$, and the iteration process does not stop until T_s is stable within 0.01 K (Van Den Broeke et al., 2005). This way of working ensures a closed energy balance. If the final T_s exceeds the melting point, it is reset to melting point (273.15 K) and Equation (1) is recalculated, with the excess energy (QM > 0) consumed for surface melting.

3.2. Turbulent Heat Flux Calculation

Based on the Monin-Obukhov similarity theory, the bulk aerodynamic method with a stability correction was applied to estimate the turbulent heat fluxes (Oke, 1987; Ruckstuhl et al., 2007). For stable conditions, the stability correction function proposed by Holtslag and De Bruin (1988) was adopted, while for unstable conditions, the scheme of Dyer (1974) was used. SH and LE were calculated as follows:

$$\mathrm{SH} = \rho_a c_p u_* \theta_* = \rho_a c_p C_H u(T - T_s), \tag{4}$$

$$\mathrm{LE} = \rho_a L_v u_* q_* = \rho_a L_v C_E u(q - q_s), \tag{5}$$

where ρ_a is the air density, c_p is the specific heat capacity of the air at constant pressure. $c_p = c_{\mathrm{pd}}(1 + 0.84q)$, where $c_{\mathrm{pd}} = 1005\ \mathrm{J\ kg^{-1}\ K^{-1}}$ is the specific heat capacity for dry air at constant pressure. L_v ($2.834 \times 10^6\ \mathrm{J\ kg^{-1}}$) is the latent heat for sublimation when $T_s < 273.15$ K or for evaporation ($2.501 \times 10^6\ \mathrm{J\ kg^{-1}}$) when $T_s = 273.15$ K (i.e., melting occurs). u_* (in m s^{-1}), θ_* (in k), and q_* (in kg kg^{-1}) are the turbulent scales for momentum, heat, and moisture, respectively. C_H and C_E are bulk exchange coefficients for SH and LE calculations, respectively (dimensionless). u (in m s^{-1}) is the measured wind speed. T (in K) and q (in kg kg^{-1}) are air temperature and specific humidity, respectively, with the subscript "s" denoting surface values. As suggested by Brock et al. (2010), Favier et al. (2004), and Wagnon et al. (2003), a saturated surface, that is, RH = 100%, is assumed at the glacier surface.

The surface roughness lengths for momentum (z_{om}), moisture (z_{oq}) and heat (z_{ot}) are indispensable variables for calculating SH and LE. Following Ding et al. (2020), z_{om} was calculated by the schemes of Holtslag and De Bruin (1988) and Dyer (1974) using the two-level wind speed measurements. As there is a substantial variability in the calculated hourly z_{om} values, the 20-day ($N = 480$) running means of hourly z_{om} proposed by van den Broeke, Smeets, and Ettema (2008) were adopted for turbulent heat calculations. Our results show that the calculated hourly z_{om} values were between 0.23 and 0.41 mm (Figure 2a), while the daily z_{om} magnitudes ranged

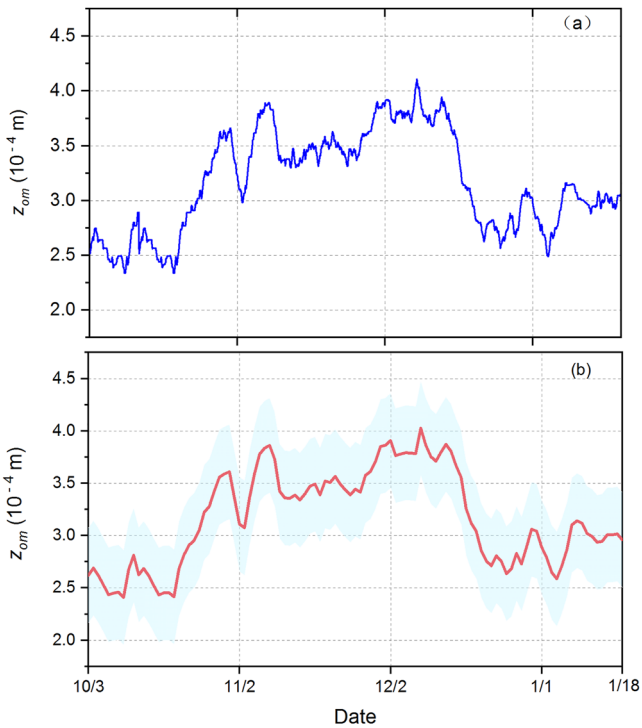

Figure 2. 20-day running surface momentum roughness means of z_{om} calculated from two-level wind speed measurements. (a) shows the hourly z_{om} values; (b) presents the daily values (red line), with the blue envelope indicating the daily $z_{om} \pm \sigma$, where σ is the standard deviation of the daily z_{om}.

0.24–0.4 mm and had a daily average of 0.32 mm with a standard deviation of 0.045 mm (Figure 2b). The z_{om} magnitude obtained here is comparable to those ever reported on the other glaciers worldwide which were summarized by Brock et al. (2006). z_{oq} and z_{ot} were calculated using the Reynolds number (Re^*) proposed by Andreas (1987).

3.3. Model Validation

Verification of the modeled against the "measured" T_s values (derived from the AWS-measured LR↑) provides an effective means to assess the performance of the glacier SEB model (Kuipers Munneke et al., 2012). Comparing all 2592 modeled and measured hourly T_s pairs (Figure 3) in this study yields a bias of −0.76 K, a root mean squared error (RMSE) of 3.4 K, and a coefficient of determination $R^2 = 0.84$. This demonstrates that the SEB model performed well, even though there was a slight T_s overestimation when the "measured" $T_s < 255$ K (generally occurring at night), but a T_s underestimation when the "measured" $T_s > 255$ K (generally occurring in the day). The possible explanation will be discussed in Section 5.

3.4. Calculating Longwave-Equivalent Cloudiness

Cloud is a valuable variable for correctly interpreting the temporal variability of radiation fluxes (van den Broeke, Smeets, Ettema, Munneke, et al., 2008) or even turbulent heat fluxes (Conway et al., 2022). To discern clouds' effect on the glacier SEB pattern, the longwave-equivalent cloudiness defined by Van den Broeke et al. (2006) was calculated to indicate the cloudiness during our observation. It is given as follows:

$$N_L = (\varepsilon_{\text{eff}} - \varepsilon_{\text{cs}})/(\varepsilon_{\text{ov}} - \varepsilon_{\text{cs}}),$$

$$N_L\,(N_L > 1) = 1, N_L\,(N_L < 0) = 0, \quad (6)$$

where N_L is longwave equivalent cloudiness and ε_{eff} is the effective emissivity of the atmosphere by rearranging

$$\text{LR}\downarrow = \varepsilon_{\text{eff}}\,\sigma\,T^4, \quad (7)$$

ε_{cs} is the effective emissivity of the atmosphere in clear skies, with the subscript cs denoting clear sky. ε_{ov} (= 1) is the atmospheric emissivity under overcast conditions. The higher the N_L is, the more cloud cover there is at the observational site. For instance, Giesen et al. (2008) and Conway et al. (2022) defined $N_L < 0.2$ as clear-sky conditions and $N_L > 0.8$ as overcast conditions, while Van den Broeke et al. (2006) chose the threshold values of 0.3 and 0.7.

ε_{cs} was calculated using the scheme of Brutsaert (1975) as this scheme is one of the best parameterizations applicable in glaciated regions (Juszak & Pellicciotti, 2013; Zhu et al., 2016). Its expression follows:

$$\varepsilon_{\text{cs}} = P1(e/T)^{1/P2}, \quad (8)$$

$P1$ and $P2$ are site-specific constants and must be recalibrated at different observational sites (Juszak & Pellicciotti, 2013; Zhu et al., 2016). Brutsaert (1975) developed his original values of $P1 = 1.24$ and $P2 = 7$, while Mölg et al. (2009) optimized $P2 = 6$ for conditions over tropical glaciers (on Kilimanjaro). Here we recalibrated $P1$ and $P2$ by rearranging the Stefan-Boltzmann equation $\text{LR}\downarrow_{\text{cs}} = \varepsilon_{\text{cs}}\sigma T^4$ using the hourly datapoints of LR↓, air water-vapor pressure e (in hPa), and air temperature T (in K)

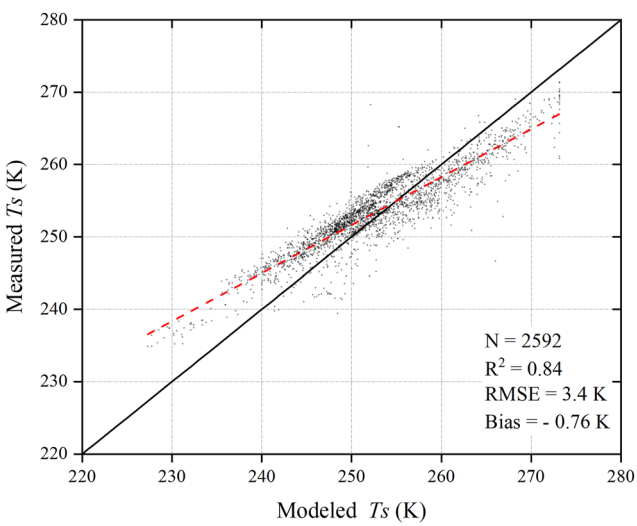

Figure 3. Modeled against the "measured" hourly T_s values. The solid black line represents the 1:1 line and the dashed red line represents the linear regression. Statistics show the number of data points (N), coefficient of determination (R^2), root mean squared error (RMSE), and bias (Bias).

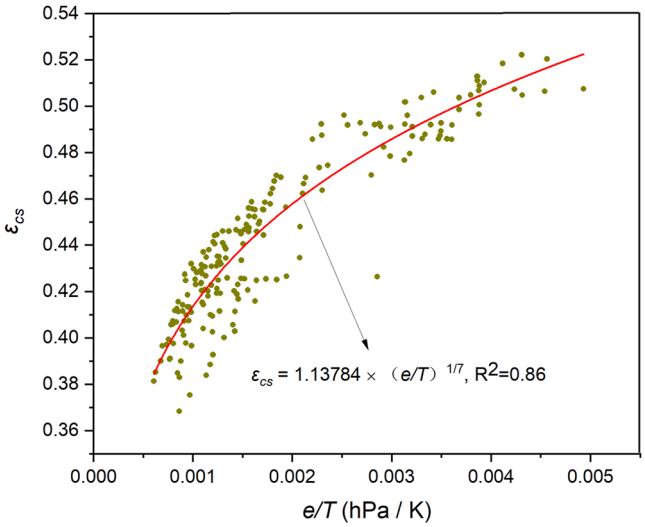

Figure 4. Recalibrated $P1$ and $P2$ for ε_{cs} parameterization for cloudless skies.

recorded by our AWS during daytime of restrictedly cloudless days. $LR\downarrow_{cs}$ indicates the LR↓ observed in clear skies. The above clear-sky hourly datapoints were selected following the criteria of Conway et al. (2015). For the 24 hourly datapoints on each day of the whole 108 days, four checking procedures were performed in sequence. First, we check whether there was a constant monotonic SR↓ increase in the morning and a subsequent decrease in the afternoon. If so, this day was regarded as clear-sky day, and all 24 hourly datapoints on it entered the following three checking procedures to see if they also meet the other three criteria: solar elevations > 29.5° in the morning and > 4.2° in the afternoon (they were calculated according to the sky-view factor in Appendix A) for eliminating the potential effect of topographic shading, RH < 90% because cloudless days with such high RH values were almost impossible (Conway et al., 2015), and no abrupt increase in "accumulated" albedo (van den Broeke, van As, Reijmer, and van de Wal, 2004) since rapid albedo increase generally indicates episodes during and immediately after snowfall events. The hourly datapoint cannot be selected as the final clear-sky hourly data until it met all of the above four criteria. Finally, we selected 200 clear-sky daylight data points, which are evenly distributed between 09:00 and 16:00 during the following four episodes: 11–14 October, 25 October–1 November, 22–28 November, and 25–30 December. The recalibration result is shown in Figure 4, with $P1 = 1.13784$ and $P2 = 7$, and thus $\varepsilon_{cs} = 1.13784 \times (e/T)^{1/7}$.

4. Results

4.1. Near-Surface Meteorological Conditions

Figure 5 shows the measured wind speed, air/surface temperatures and moistures along with their gradients above the glacier surface, and Table 2 lists their monthly values. The observed wind directions and frequencies are shown in Figure 6. The most remarkable feature of the meteorological variables is the noticeably high wind speeds at this high-altitude site. The average wind speed measured at the 4 m height was 10.8 m s^{-1}, while its hourly maximum reached as high as 29.6 m s^{-1} (at 13:00 on 11 December, local time). Wind directions were dominated by south and south-southwest and maintained a high directional constancy (Rodrigo et al., 2012; Van den Broeke & Lipzig, 2003) of 0.91. This could be explained by the substantial influence of the surrounding topography (Lang & Barros, 2004), as stated in Section 2.

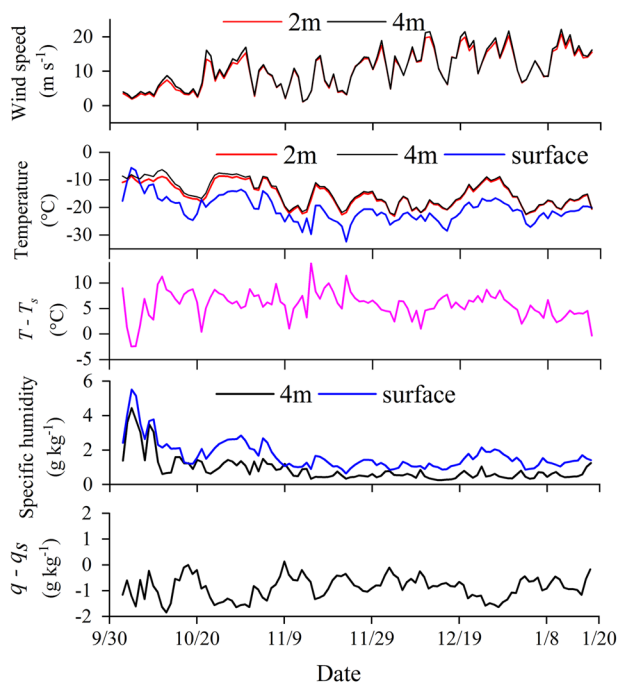

Figure 5. Daily meteorological variables recorded by the AWS.

The surface temperature fluctuated synchronously with the air temperature; on average, it was 5.7°C lower (−20.5°C vs. −14.8°C) than the air temperature. This suggests that there was a sustained temperature inversion across the layer of the near-surface atmosphere. The minimum and maximum of the hourly air temperature at the 4 m height were recorded at −26.4°C (07:00 on December 4, local time) and −3.3°C (15:00 on 8 October, local time), respectively. In response to this low temperature, the observed air specific humidity was 0.9 g kg^{-1} on average, 0.8 g kg^{-1} lower than that at the glacier surface (q_s) and indicative of a RH close to 50%.

4.2. Surface Energy Balance Results

4.2.1. Radiation, Albedo, and Cloudiness

Variations in radiation, albedo, and cloudiness are shown in Figure 7. Following the decline of the solar radiation at the top of the atmosphere (STOA), SR↓, SR↑, and SRnet all displayed gradually decreasing trends, with their daily mean values across the whole observational period being 211 W m^{-2},

Table 2
Monthly Values of the Meteorological Elements and Energy Components

Elements	October[a]	November	December	January[b]	Whole period
Air pressure (hPa)	459	456	453	452	455
T (°C)	−10.1	−15.6	−16.2	−18.6	−14.8
T_s (°C)	−15.9	−22.6	−21.9	−22.3	−20.5
$T - T_s$ (°C)	5.8	7.0	5.7	3.7	5.8
q (g kg^{-1})	1.6	0.7	0.5	0.6	0.9
$q - q_s$ (g kg^{-1})	−1.0	−0.8	−0.9	−0.7	−0.9
Wind speed (m s^{-1})[c]	7.4	8.2	14.9	13.7	10.8
Cloud coverage	0.16	0.10	0.13	0.30	0.15
Surface albedo	0.73	0.69	0.67	0.65	0.69
SR↓ (W m^{-2})	272	220	178	152	211
SR↑ (W m^{-2})	−195	−151	−117	−97	−144
LR↓ (W m^{-2})	147	116	115	136	127
LR↑ (W m^{-2})	−242	−219	−220	−218	−225
SRnet (W m^{-2})[d]	77 (65%)	69 (58%)	61 (45%)	56 (54%)	67 (55%)
LRnet (W m^{-2})[e]	−91 (76%)	−99 (83%)	−101 (74%)	−78 (75%)	−94 (77%)
Rnet (W m^{-2})	−13	−30	−40	−23	−27
SH (W m^{-2})[f]	36 (30%)	48 (40%)	75 (55%)	47 (45%)	52 (43%)
LE (W m^{-2})[g]	−26 (22%)	−21 (18%)	−36 (26%)	−26 (25%)	−27 (22%)
G (W m^{-2})[h]	6 (5%)	3 (3%)	1 (1%)	1 (1%)	3 (2%)
QM (W m^{-2})	−3 (0)	0 (0)	0 (0)	0 (0)	−1 (0)
Westerlies index (gpm)	109	112	144	164	129
Wind speed from ERA5 (m s^{-1})[i]	7.7	8.4	15.5	14.7	11.3

[a]3–31 October. [b]1–18 January. [c]Observed values at 4 m high. [d–h]Percentages in bracket denote the contributions to the total energy source of SRnet, SH, and G, and the contributions to total energy sink for LRnet, LE, and QM. [i]The zonal wind speed at the 460 hPa level in the ERA5 grid of the AWS's location.

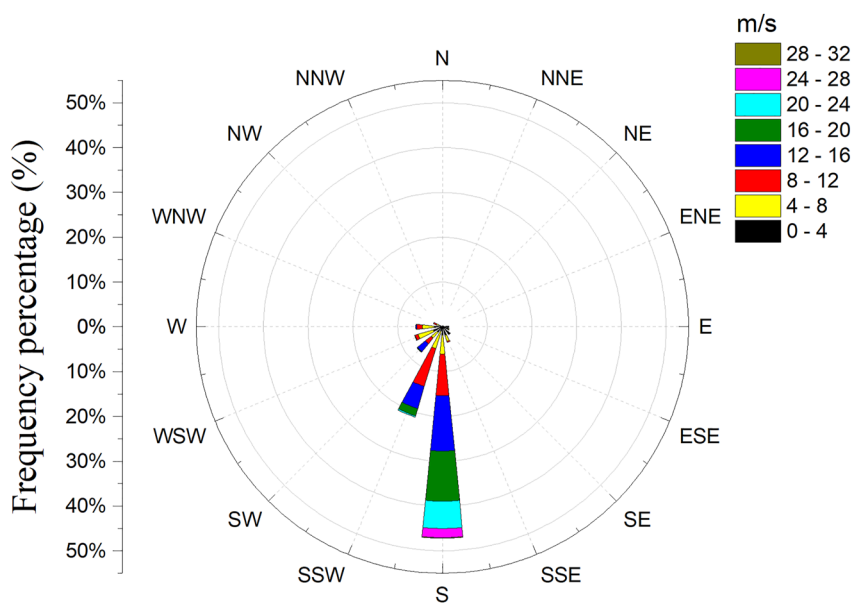

Figure 6. Wind direction and its frequency observed by the AWS.

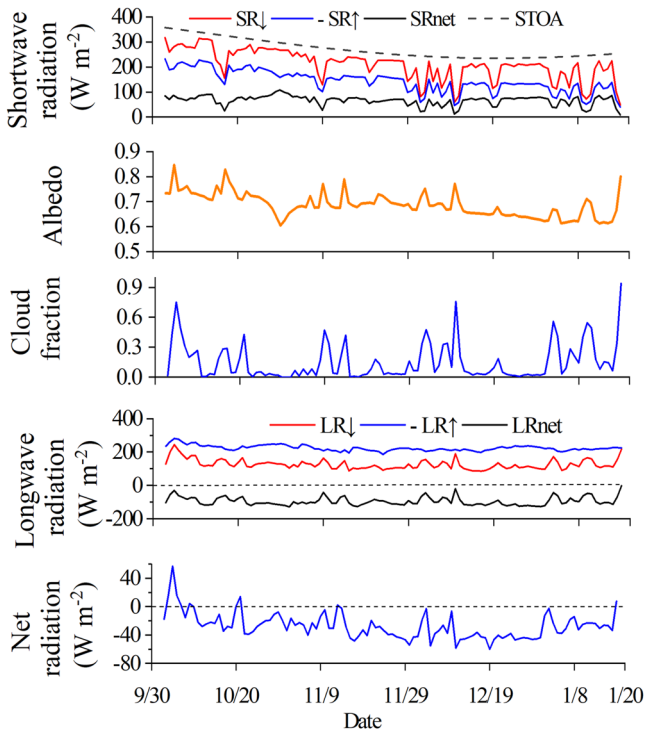

Figure 7. Variations in the observed daily radiation components, albedo, and cloudiness.

−144 W m^{-2}, and 67 W m^{-2}, respectively. Radiative fluxes showed substantial variability in the following five episodes: 4–10 October, 8–9 November, 29 November–10 December, 19–20 December, and 2–18 January. This can be explained by the possible passage of synoptic systems, which would induce a large number of clouds and thus reduce atmospheric transmission (Pellicciotti et al., 2011), eventually resulting in a decrease in SR↓ and consequent reductions in SR↑ and SRnet.

Daily albedo varied from 0.60 (on October 30) to 0.85 (on October 5), with an averaged value of 0.69. This is a remarkably low value for dry, clear snow, and was most possibly induced by dust sedimentation and snow metamorphism. In addition, albedo varied nearly simultaneously with the cloudiness. This can be explained by (1) clouds can fundamentally change the spectral composition of SR↓ toward shorter and higher albedo wavelengths (Grenfell et al., 1981; W. Wang et al., 2018), and (2) the occasional increase in cloudiness is typically indicative of snowfall, which usually caused abrupt increases in surface albedo.

According to the Stefan-Boltzmann equation (LR↑ = 0.97 σT_s^4), variation in the surface-emitted LR↑ is dependent on the changes in T_s. As the daily T_s varied around −21°C (Figure 5), LR↑ was close to −225 W m^{-2}, with a relatively small standard deviation of 16 W m^{-2}. In contrast, daily LR↓ had a high amplitude, ranging from 87 W m^{-2} to 245 W m^{-2} with a larger standard deviation of 29 W m^{-2}. Clouds, integrated amount of water vapor, and atmospheric temperature are three variables impacting LR↓ (Gubler et al., 2012), all of which experienced rapid changes in this study (Figure 5). As expected, higher air specific humidity and more cloudiness, which can enhance sky emissivity significantly (Sicart et al., 2010), were generally associated with larger LR↓ (Figure 7). For instance, during 7–9 November, when air specific humidity increased from 0.9 g kg^{-1} to 1.2 g kg^{-1} and cloudiness increased from 0 to 0.5, LR↓ increased from 113 W m^{-2} to 164 W m^{-2}; in comparison, over the following three days when air specific humidity and cloud cover decreased from 0.8 to 0.5 g kg^{-1} and from 0.5 to null, respectively, LR↓ decreased from 139 W m^{-2} to 100 W m^{-2}. Similar notable LR↓ variations were also observed over 14–8 October, 28 November to 20 December, and 1-18 January.

The daily net longwave radiation (LRnet = LR↓ + LR↑) was consistently negative, indicating that LRnet was a continuous energy sink for the glacier surface. Although the magnitude of LRnet occasionally exceeded SRnet, it was 27 W m^{-2} greater in magnitude averagely than SRnet (−94 W m^{-2} vs. 67 W m^{-2}), which led to a net radiation loss of 27 W m^{-2} (i.e., Rnet = LRnet + SRnet = −27 W m^{-2}) on average. This indicates that the glacier surface experienced quasi-continuous radiative cooling, a typical phenomenon of a "cold" snowpack receiving low solar radiation during the boreal cold winter (Oke, 1987). This is the combined result of several factors, including the large solar zenith angle that induced small incident solar radiation, the high albedo of the glacier that allowed highly reflected SR↓ and thus weak surface absorption of SR↓, and the deficient clouds that have a great ability to decrease LR↓ and thus led to a substantial LRnet loss.

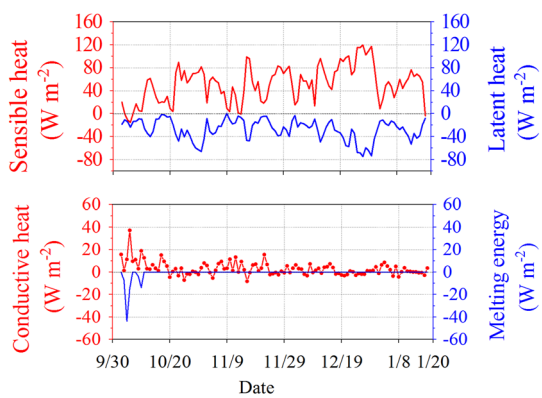

Figure 8. Variations in daily SH, LE, G, and QM.

4.2.2. Turbulent and Subsurface Heat Fluxes

The daily variations in the turbulent (SH and LE) and subsurface heat (G) fluxes are shown in Figure 8. As a result of the temperature inversion above the surface (see Section 4.2 and Table 2), mixing commonly transfers sensible heat toward the glacier surface, warming the glacier surface (Cuffey & Paterson, 2010). Because of the noticeably high wind speed (10.8 m s^{-1}) and the significant temperature inversion (5.8°C, Table 2), the magnitude of SH was high, with its daily average being as large as 52 W m^{-2}. The vertical temperature gradient went from 5.8°C to 7.0°C and then 5.7°C from September to December, while wind speeds during this period increased significantly from 7.4 m s^{-1} to 14.9 m s^{-1}, eventually causing a substantial

SH increase from 36 W m^{-2} to 75 W m^{-2}. This highlights the significant role of wind speed in the turbulence exchange. The peak daily SH was observed at 120 W m^{-2} on 27 December. This was resulted from a rare combination of intense temperature inversion and the highest wind speed (19.7 m s^{-1}), reminiscent of the interior of the large ice sheets where katabatic winds are active. The strong SH transport would warm the glacier surface, accelerating snow metamorphism and eventually decreasing the surface albedo.

Daily LE was persistently away from the glacier surface because of the lower moisture content in the near-surface layer than at the glacier surface. As a result, LE served as a continuous energy sink for the glacier surface, inducing an unintermittent surface energy/mass loss through sublimation and moistening of the atmosphere. LE has a daily average of −27 W m^{-2}, implying an averaged sublimation-driven surface mass loss of 0.8 mm (0.8 ± 0.5 mm) water equivalent (w.e.) per day, a magnitude almost equivalent to that obtained at 7,945 m asl, South Col of Qomolangma (Matthews et al., 2020). Due to the exceptionally high wind speed (19.7 m s^{-1}), LE reached its daily maximum of 75 W m^{-2} on 27 December, indicating a maximum sublimation loss of 2.2 mm w.e. on this day. This helped to explain the surface's highly metamorphosed state (Colbeck, 1983; Domine et al., 2003; Ebner et al., 2015; Hansen & Foslien, 2015) as well as the relatively low surface albedo, as observed in this study.

G contributed 3 W m^{-2} to the glacier SEB on average, although both positive and negative daily G at the sub-daily time scale were observed every day. The positive G indicates a subsurface heat transfer from the deeper layer to the surface, warming the glacier surface and raising T_s, and vice versa. The daily maximum was observed at 37 W m^{-2} on 6 October, a day with the daily T_s higher than T and thus with an upward SH. Melting energy maintained zero throughout the observational period except for five relatively warm days in early October.

4.2.3. Average Surface Energy Budget at the Glacier Surface

The glacial surface energy balance is listed in Table 2. SRnet (67 W m^{-2}) contributed the most of the energy source (55%), followed by SH (52 W m^{-2}) and G (3 W m^{-2}) with their shares being 43% and 2%, respectively. Among the energy sinks, LRnet (−94 W m^{-2}) contributed the largest portion (77%), followed by LE (−27 W m^{-2}) with a contribution of 22% and QM (−1 W m^{-2}) with a minor portion of only 1%.

4.2.4. Diurnal Cycles of the Surface Energy Balance

Figure 9 shows the diurnal cycles of the glacier SEB and the associated meteorological variables under different cloudiness conditions. In general, all SEB components showed comparable diurnal variations, with a significant change in the day but minimal variability at night. Following the variability in SRnet, the other energy components (LRnet, Rnet, SH, LE, and G) and the related meteorological variables (q, T, T_s, and u) increased in the morning, peaked at around 14:00, but subsequently decreased until the early night (20:00).

However, when cloudiness appeared, the above diurnal cycles were disturbed, and the amplitude of SEB components got smaller and the fluctuations in q, T, T_s, and u became irregular. When the cloudiness N_L was less than 0.2, for instance, SRnet, LRnet, and Rnet had amplitudes that were, respectively, 222, 24, and 175 W m^{-2} higher than those when the cloudiness N_L was larger than 0.8. Similarly, the diurnal amplitudes of SH and LE were 93 W m^{-2} and 52 W m^{-2} higher in the case of $N_L < 0.2$ than those when $N_L > 0.8$. However, G did not vary much with the change in clouds.

The negative Rnet at night but positive Rnet during the day indicates that the surface cooled at night but was warmed during the day. Relative to the daytime SH, SH at night was higher because the rise of near-surface vertical temperature gradient at night (from the daytime 1°C to 5°C at night) exceeded the reduction in wind speed (from 9.7 m s^{-1} in the day to 9.2 m s^{-1} at night). Between 13:00 and 16:00, SH switched from downward to upward, which is indicative of the shifting of the near-surface atmosphere stability from an almost all-day stable condition to an unstable condition. This would potentially induce convection in the near-surface atmosphere. However, because the vertical temperature gradient was small, the strength of the convection was restrained, thus resulting in a weak SH. As the surface is assumed to be saturated, q_s followed T_s and was always higher than q, resulting in persistently negative day-round LE with a peak value at 15:00.

At 10:00 o'clock, as a response to the SR↓ absorption by the glacier surface, T_s increased and G switched its direction from upward to downward before shifting back to upward at 17:00. Compared to the relatively small daily magnitude, G at the sub-daily time scale was higher. This can be explained by the fact that snow is a poor heat conductor, allowing a rapid T_s adjustment to the surface radiative forcing and thus leading to a significant subsurface temperature gradient and thus high G magnitude at the sub-daily time scale.

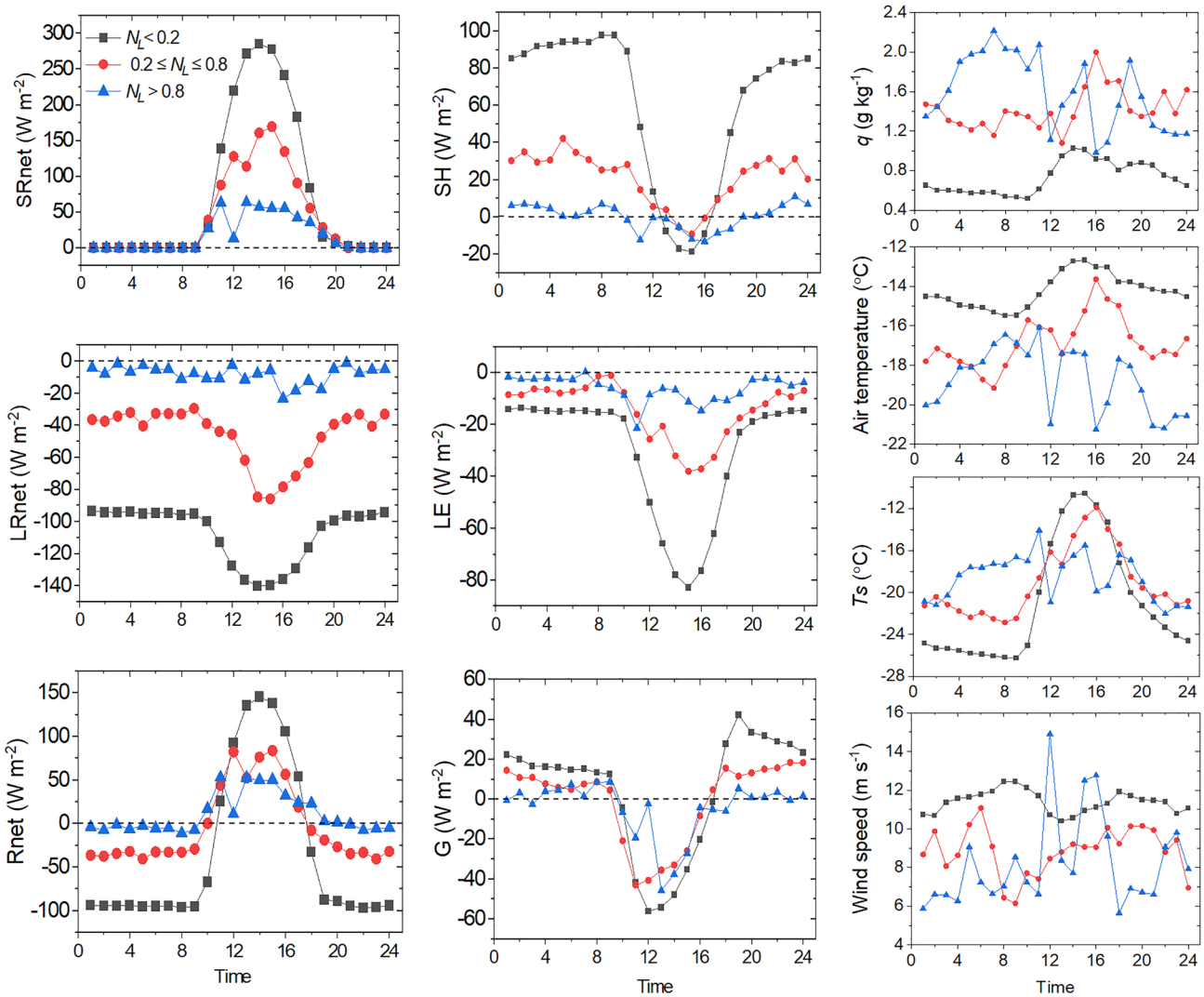

Figure 9. Diurnal SEB cycles and associated meteorological variables under different longwave equivalent cloudiness N_L.

4.3. Phenomenological Link Between SEB and Synoptic System

Variations in the SEB components during 7–10 December and the associated synoptic systems are taken as an example here to illustrate their phenomenological link because these 4 days experienced the most frequent and notable variations in SR↓, which suggests possible passing of synoptic systems.

According to the geopotential height fields at the 450-hPa level (Figures 10a, 10c, 10e, and 10g), a large-scale low-pressure system passed during the four days. Most of the area around Mt. Qomolangma was influenced by this low-pressure system, with its southern edge close to the mountain. This situation is comparable to that documented by Lang and Barros (2004) who claimed that low temperatures or even winter snowstorms are frequently linked to terrain-locked low-pressure systems in the Himalayas. On 7 December, a cold front moving eastward passed Mt. Qomolangma (Figure 10b) with a steady southwest wind accompanying it near the AWS (Figure 10a). This resulted in a notable decrease in air temperature (−16°C to −20°C) but significant rises in specific humidity (0.3–1.2 g kg^{-1}), wind speed (8.0 m s^{-1} to 14.9 m s^{-1}), cloudiness (0.1–0.9), and LR↓ (120–223 W m^{-2}) (Figure 11). On 8 December, a weak trough of low pressure (Figure 10c) allowed cold air from the northwest (Figure 10d), causing the air specific humidity (from 1.2 g kg^{-1} to 0.2 g kg^{-1}) and the temperature (from −20°C to −22°C (Figure 11)) to drop further. On 9 December, as the low-pressure system advanced, the southwest wind near Mt. Qomolangma was once more predominated (Figure 10e); air temperature and moisture increased slightly (Figure 11), but cloudiness remained nearly unchanged until the evening when a notable increase occurred as evidenced from the increase in LR↓ (128–205 W m^{-2}). On 10 December, the meteorological elements underwent the most noticeable fluctuation.

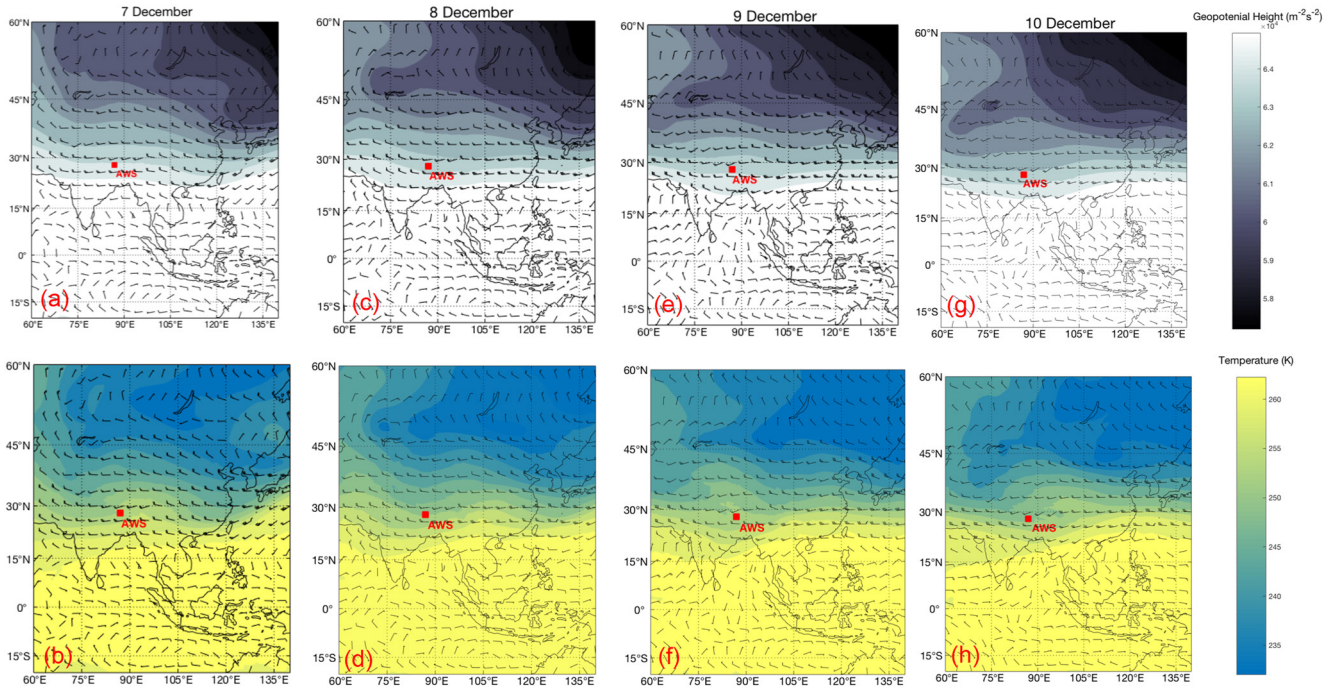

Figure 10. Geopotential height fields ((a), (c), (e), and (g)) and temperature fields ((b), (d), (f), and (h)) at the level of 450 hPa during 7–10 December 2007. Also included are the wind fields, with the wind speeds indicated by Beaufort scale.

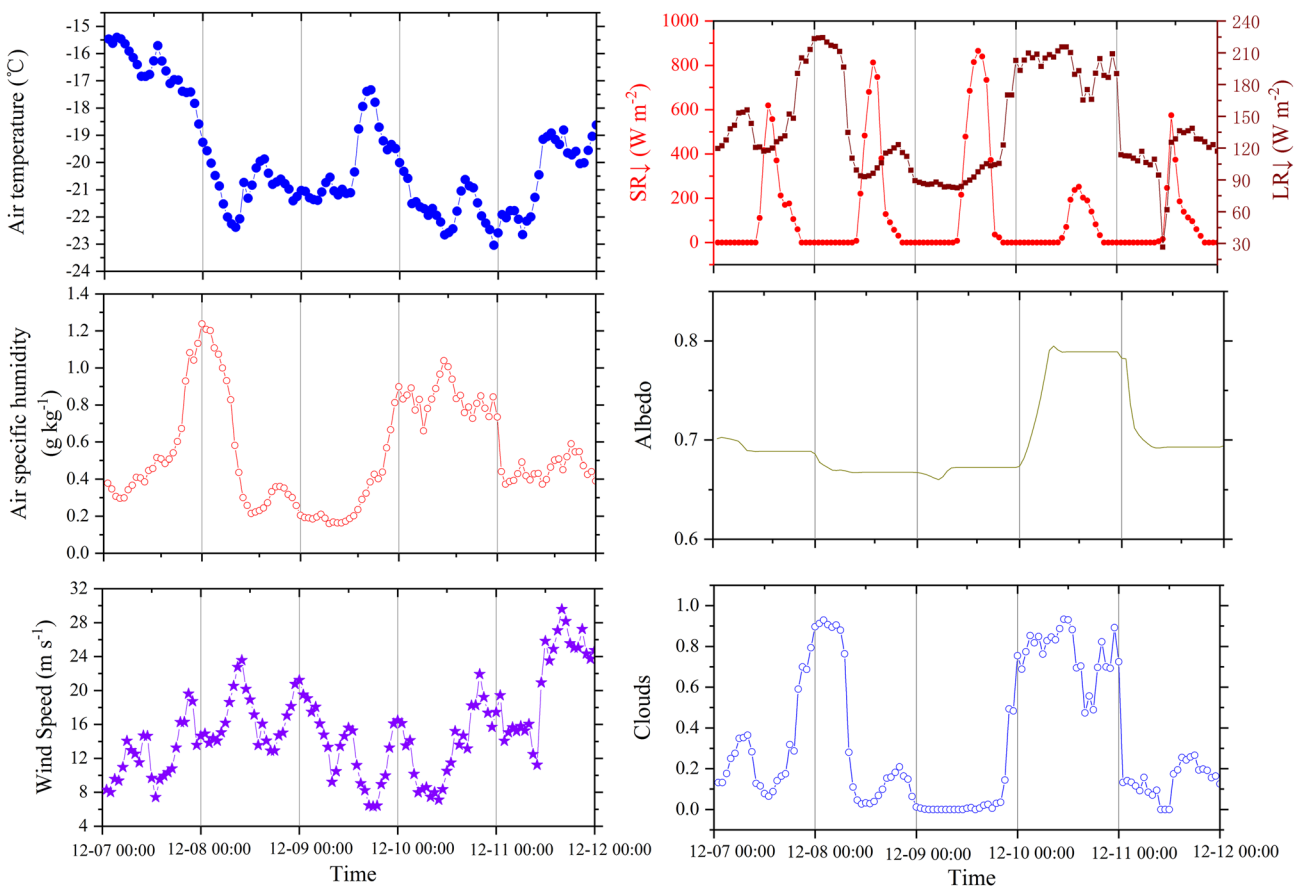

Figure 11. Variations in the meteorological variables and the incoming radiations during the synoptic weather system passing during 7–10 December 2007.

Table 3
Comparison of Seasonal Meteorological Variables and SEB Components (W m^{-2}) Between the Cold and Warm Seasons, Respectively

Elements	T_s (°C)	T (°C)	$T - T_s$ (°C)	q (g kg^{-1})	$q - q_s$ (g kg^{-1})	Wind speed (m s^{-1})	Cloud	Albedo	STOA	SR↓	SR↑	LR↓	LR↑	SRnet	LRnet	Rnet	SH	LE
Cold season[a]	−20.5	−14.8	5.8	0.9	−0.9	10.8	0.15	0.69	271	211	−144	127	−225	67	−94	−27	52	−27
Warm season[b]	−9.8	−7	2.8	3.4	−1.1	4.2	0.44	0.72	484	366	−259	208	−274	107	−66	40	12	−20

[a]The observation covers the period from 3 October 2007 to 18 January 2008, during which the air temperature/humidity and wind speed were measured at 4.0 m. [b]Warm season indicates the period from 3 May to 22 July 2005, during which the low-level air temperature/humidity and wind speed were recorded at 1.5 m.

On this day, the area around Qomolangma was affected by a southwesterly wind (Figure 10g), which, in combination with the influence of a cold air advection (Figure 10h), resulted in a noticeable decrease in air temperature (−20°C to −23°C in Figure 11). Moreover, because of the confluence of the moisture from the southwest and cold air advection, cloudiness maintained high, resulting in an extremely low SR↓ (61 W m^{-2}) but a relatively high LR↓ (198 W m^{-2}) (Figure 11); Meanwhile, SH (14 W m^{-2}) and LE (−9 W m^{-2}) reached their lowest magnitudes, while the albedo (0.77) on this day was higher than any of the previous three days. Our result here is in line with that of Lai et al. (2021) who suggested that the synoptic weather system significantly impacts the atmosphere boundary on TP.

5. Discussion

5.1. Comparison With the Warm-Season Surface Energy Balance

To detect whether there is a difference between the cold- and warm-season glacier SEBs, we compared the glacier SEB result obtained here with that over the warm May-July season presented in W. Liu et al. (2021). The comparison result is listed in Table 3. Attributed to the higher solar zenith angle, STOA in this study was 213 W m^{-2} lower than that in the warm season (271 W m^{-2} vs. 484 W m^{-2}), which, to a large extent, can explain the lower SR↓ magnitude in this study (211 W m^{-2} in the cold season vs. 366 W m^{-2} in the warm season). Second, because of the low frequency of precipitation (14%, see Section 2) and the intense snow metamorphism induced by substantial sublimation, the surface albedo in this study was 0.03 lower than that in the warm season, which, combined with deficient cloudiness, would potentially lead to increased absorption of SR↓ (higher SRnet) by the glacier surface; however, instead of increasing, SRnet decreased by 40 W m^{-2} in the cold season. This can be explained by the fact that the increase in SR↓ absorption, potentially induced by reductions in both albedo and cloudiness, did not offset the significant decrease in STOA.

The longwave radiation in the cold season was smaller than the counterpart in the warm season, with LR↑ and LR↓ 49 W m^{-2} and 81 W m^{-2} lower in magnitude than those in the warm season. The smaller LR↓ values in the cold season can be attributed to the decreased cloudiness (T. Zhang et al., 1996) (0.15 vs. 0.44), colder atmosphere (−14.8°C vs. −1°C), and smaller total column water vapor content above the glacier surface (Duguay, 1993; T. Zhang et al., 1997) which can be indicated by the lower air specific humidity (0.9 g kg^{-1} vs. 3.4 g kg^{-1}). In comparison, the reduced LR↑ in the cold season was ascribed to the lower surface temperature (10.7°C lower in the cold season than in the warm season). Additionally, attributed to the higher LR↓ decrease compared to the LR↑ reduction, LRnet in the cold season was more negative than that in the warm season, implying a larger longwave radiation loss in the cold season. Combined with the reduced shortwave radiation absorption, this resulted in the Rnet shifting to −27 W m^{-2} in the cold season from the warm-season value of +40 W m^{-2}.

SH in this study increased by over 400% compared to the warm season (52 W m^{-2} vs. 12 W m^{-2}). This is due to the significant increases in both the wind speed (10.8 m s^{-1} vs. 4.2 m s^{-1}) and the vertical temperature gradient above the surface (5.8°C against 2.8°C). However, LE only experienced a slight increase of 7 W m^{-2} in the cold season. This can be explained by the fact that the decrease in LE potentially induced by the reduction in moisture gradient (0.9 g kg^{-1} vs. 1.1 g kg^{-1}) was partially offset by the increase in the wind speed.

5.2. Quantifying the Clouds-Induced Radiative Fluxes

Clouds have a significant impact on glacier SEB (Conway et al., 2015; Litt et al., 2019) because they can simultaneously alter LR↓ and SR↓, which are typically the two primary energy sources for surface melting on the majority of glaciers worldwide (Sicart et al., 2008). At the highly reflective glacier surface and under the influence

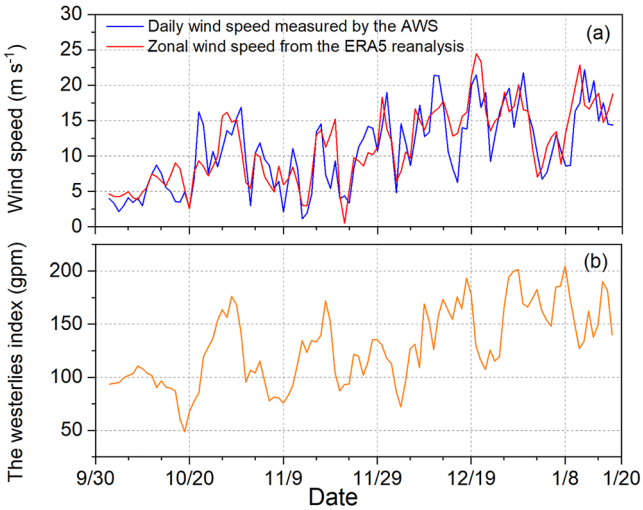

Figure 12. Variations in the westerlies index, wind speeds measured by AWS and from the ERA5 reanalysis.

of the clouds, "radiation paradox" (Ambach, 1974) generally happens, that is, net radiation increases with the increased cloudiness. Section 4.2.4 has qualitatively described how clouds affect the glacier SEB. However, the precise degree to which clouds have changed SR↓ and LR↓ is still unknown. To quantitatively assess the clouds' impact on the downward radiations, the accurate SR↓ and LR↓ magnitudes induced by clouds are quantified in this section. Here, we only present the quantification result, while the detailed methodology is presented in Appendix A. Our results show that clouds decreased SR↓ by 41 W m^{-2} but increased LR↓ by 16 W m^{-2} on average, thus leading to an overall decrease in the incoming radiation by 25 W m^{-2}. This suggests that the clouds' shading effect surpassed its greenhouse effect during our observation.

Clouds change the nature and magnitude of SR↓ from STOA in a more fundamental and often larger way than other atmospheric components such as ozone, aerosols, water vapor, and minor gases (Augustine & Hodges, 2021; van den Broeke, Smeets, Ettema, Munneke, et al., 2008). They not only limit atmospheric transmissivity for shortwave radiation and thus reduce SR↓ but also increase glacier albedo and thus decrease the shortwave radiation absorption by the glacier surface (van den Broeke, Reijmer, & van de Wal, 2004). In addition, clouds absorb thermal infrared radiation emitted by the glacier surface and the lower atmosphere, increasing the longwave radiation back to the surface (T. Zhang et al., 1997).

5.3. Effect of the Westerlies' Strength on Turbulent Sensible Heat Flux

TP significantly affects atmospheric circulation through thermal and dynamical effects (B. Wang, 2006; Wu et al., 2015). As a huge obstacle, it splits the wintertime westerlies into the northern and southern branches, with the latter establishing in mid-October (Beesley, 2000). Previous research conducted at 5050 m asl on the northern slope of Mt. Qomolangma demonstrated that the winter westerlies' downward momentum generates strong near-surface winds and thus induces significant sensible heat fluxes on the loamy sand surface (Zou et al., 2009). However, the westerlies' impact on high-altitude glacier surface has been rarely discussed.

To investigate the westerlies' impact on the turbulent sensible heat on the glacier surface at the 6,523 m asl, the westerlies' index (in unit of geopotential height, gpm hereafter) developed by L. Li et al. (2020) using the EAR5 reanalysis at the 450 hPa level was adopted here to describe the intensity of the westerlies. In addition, the ERA5 zonal wind speed (m s^{-1}) at the grid point where our AWS is located is also selected as another index to indicate the strength of the westerlies.

Figure 12 shows that during the episode prior to mid-December, the AWS-recorded and the ERA5 wind speeds are almost synchronous with the westerlies' index, but during the following period, this synchronicity became weak or even disappeared. Along with the westerlies index increasing from 109 gpm in October to 164 gpm in January, the AWS-recorded wind speeds increased from 7.4 m s^{-1} in October to 14.9 m s^{-1} in December but then to a slightly reduced magnitude of 13.7 m s^{-1} in January, while the EAR5 zonal wind speeds increased from 7.7 m s^{-1} in October to 15.5 m s^{-1} in December but then to a slightly lower value of 14.7 m s^{-1} in January (Table 2). The aforementioned wind speed increase resulted in SH increasing from 36 W m^{-2} in October to 75 W m^{-2} in December and then to a slightly smaller value of 47 W m^{-2}. In comparison, LE only increased by a small magnitude (Table 2). Our findings are consistent with Lai et al. (2021), who suggested that the westerlies can cause high near-surface wind speeds and increase the turbulent heat fluxes.

5.4. Uncertainty Evaluation

Uncertainty may exist in turbulent heat calculations. In line with Brock et al. (2010), Favier et al. (2004), Sicart et al. (2005), and Wagnon et al. (2003), it was evaluated by adding perturbations to the conventional variables utilized for turbulent heat calculation, such as air temperature, RH, sensor height, and z_{om}. Table 4 shows that when air temperature changed by 1°C, SH varied by 2%–13% and LE changed by 4%–19%; when RH changed

Table 4
Sensitivity of the Turbulent Heat Fluxes to Changes in Conventional Variables

Parameters	ΔSH	ΔLE
Control	52 W m^{-2}	−27 W m^{-2}
T + 1°C	+2%	+19%
T − 1°C	−13%	−4%
RH + 5%	−2%	−3%
RH − 5%	0	0
u + 1.5 m s^{-1}	+4%	+26%
Z + 0.5 m	−8%	+7%
Z − 0.5 m	−6%	+15%
10 z_{om}	+4%	+26%
z_{om}/10	−23%	−15%
SR↓ ±5%	−6%	+11%
SR↑ ±5%	−4% to −12%	+8% ~ 15%

by 5%, SH and LE varied by no more than 3%; if wind speed increased by 1.5 m s^{-1}, SH and LE increased by 4% and 26%, respectively; and when observation height changed by 0.5 m, SH and LE varied by about 10%. Using z_{om}/10 and 10 × z_{om} would change SH by −23%–4% and LE by −15%–26%. Given the measurement accuracy of the pyranometer (5%) (van den Broeke, van As, Reijmer, & van de Wal, 2004), a perturbation of 5% for SR↓ resulted in SH and LE changes by −6% and +11%, respectively; A disturbance of 5% for SR↑ led to fluctuations of −4% to −12% for SH and +8% to +15% for LE, respectively. In summary, z_{om} appears to cause a greater turbulent heat fluctuation than the other variables. Therefore, it should be carefully chosen in glacier SEB study.

In the validation of the glacier SEB model (Section 3.3), we have shown that T_s was underestimated in the daytime but overestimated at night. This, to a large extent, means that more (less) energy should be, but in fact was not, inputted into the glacier surface for glacier SEB calculation in the daytime (at night). In other words, during the model run, the glacier surface received less energy input during the day but more energy at night. The less energy during the day likely resulted from the traditional "unconditioned" method for global and diffuse pyranometer measurements. This method will induce a higher detector temperature than the dome (Philipona, 2002; Sanchez et al., 2015), generally leading to a solar irradiance underestimation by over tens of W m^{-2} (Bush et al., 2000; Ji & Tsay, 2009; Ji et al., 2011) and thus resulting in a T_s underestimation. In contrast, the more energy input at night may be induced by the potential drifting-snow layers, which can readily form in high-wind conditions and behave as a cloud layer, increasing LR↓ (Le Toumelin et al., 2021) and thus inducing a T_s overestimation at night. It should be mentioned that the knowledge of atmospheric control on the glacier SEB obtained here may be not universal as the findings of this study are based on a site-specific and short-term observation of only 3.5 months. For a better understanding of the climatic control on the cold-season glacier SEB on Mt. Qomolangma, long-term in situ meteorological observations are needed in future.

6. Conclusions

Based on the in-situ measured meteorological data collected from 3 October 2007–18 January 2008, we investigated the cold-season glacier SEB at 6523 m asl on the northern slope of Mt. Qomolangma and identified its atmospheric control. Our results show that net shortwave radiation was the primary energy source, followed by turbulent sensible heat and a tiny portion of subsurface heat; net longwave radiation and turbulent latent heat were two energy sinks. Melting energy was not significantly different from zero. There was a high wind speed, with its daily value usually exceeding 10 m s^{-1}, which, in combination with deficient clouds, led to a substantial sensible heat transport toward the glacier surface and thus enhanced the outgoing longwave radiation and the net longwave radiative loss. Combined with the high albedo of the glacier surface and the low STOA in the cold season, this led to a semi-permanent radiative deficit and thus a surface radiative cooling. Quantitative analysis demonstrates that clouds decreased the incident shortwave radiation more than increased the incoming longwave radiation, leading to an overall decrease in the downward radiation, which implies that the clouds' shading effect surpassed its greenhouse effect. This study provides valuable insights into glacier energy/mass exchanges in the cold season at such a high altitude on the northern slope of Mt. Qomolangma, which would help to better understand the distinct glacier changes when the local climate is affected by the westerlies.

Appendix A

The magnitudes of LR↓ and SR↓ altered by clouds are the radiation differences between the all-sky and clear-sky days (Intrieri, 2002). Under the common assumptions of (a) unchanged meteorological conditions between all-sky and clear-sky conditions (W Wang et al., 2018) and (b) an instantaneous clouds' effect on radiative fluxes (Ramanathan et al., 1989), the clouds-altered radiations are expressed as:

$$\Delta LR\downarrow = LR\downarrow - LR\downarrow_{cs}, \quad \text{(A1)}$$

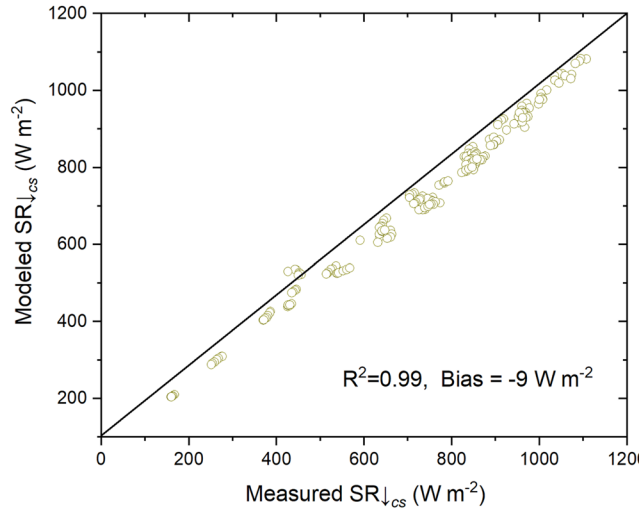

Figure A1. Modeled versus measured hourly $SR\downarrow_{cs}$ values.

$$\Delta SR\downarrow = SR\downarrow - SR\downarrow_{cs}, \tag{A2}$$

where $\Delta LR\downarrow$ and $\Delta SR\downarrow$ are the clouds-altered incoming longwave and shortwave radiative fluxes; $LR\downarrow_{cs}$ and $SR\downarrow_{cs}$ are incoming longwave and shortwave radiations in clear skies, which can be estimated using clear-sky radiation models. Here, the $LR\downarrow_{cs}$ was modeled using the Stefan-Boltzmann equation $LR\downarrow_{cs} = \varepsilon_{cs}\sigma T^4$, with $\varepsilon_{cs} = 1.13784 \times (e/T)^{1/7}$ as previously calibrated in Section 3.4.

For the $SR\downarrow_{cs}$ estimation, the model of Bird and Hulstrom (1981) was used as it had the best performance in a model comparison study by Annear and Wells (2007). In addition, it also shows good performance on TP's glaciers (Chen et al., 2018). The basic expression of this model is $SR\downarrow_{cs} = S_{cs} + D_{cs}$, where S_{cs} is the direct beam solar radiation, and D_{cs} is diffuse solar radiation. S_{cs} is expressed as:

$$S_{cs} = 0.9751 S_0 E_0 \tau_{cs} \sin h, \tag{A3}$$

where 0.9751 is the ratio of solar to extraterrestrial radiation, S_0 is the solar constant (1367 W m^{-2}), E_0 is the eccentricity correction factor, h is the solar elevation above the plane of the horizon. τ_{cs} represents the extinction of solar radiation by Rayleigh scattering (τ_r), absorption by gases (τ_g) and water vapor (τ_w), and attenuation by aerosols (τ_a), among which τ_r, τ_g, and τ_a were calculated using optical air mass and air pressure, and τ_w was derived from the optimal air mass and precipitable water (Prata, 1996). The total vertical column ozone was set to be 0.294 cm, an annual average obtained over the entire TP (Zou, 1996). $\tau_a = x^m$ where m is optical air mass and x is the ratio of AWS-measured $SR\downarrow$ to predicted $SR\downarrow_{cs}$ excluding aerosol effects (Conway et al., 2015) and was optimized at 0.99 here.

D_{cs} is composed of two components, one from the clear sky and the other from solar radiation reflected from the surrounding terrain (D_t). D_{cs} from the sky was calculated as the sum of contributions from Rayleigh scattering (D_r), aerosol scattering (D_a), and multiple reflections between the surface and atmosphere (D_m) following the original expressions of Bird and Hulstrom (1981):

$$Dcs = (D_r + D_a + D_m)\,svf + D_t\,(1 - svf), \tag{A4}$$

where D_t was calculated as $D_t = \alpha_t\, SR\downarrow$. α_t is the albedo of the surrounding terrain and was set to 0.69 (the averaged AWS-measured albedo) as our AWS was located in a firn basin. Svf is the sky-view factor (Oke, 1987) and was calculated as 0.98 using a 30 m × 30 m digital elevation model (download from https://www.usgs.gov) following the shadow casting algorithm of Lindberg (2005).

To verify the robustness of the $SR\downarrow_{cs}$ model at our AWS site, we compared the modeling result of $SR\downarrow_{cs}$ for the selected 200 cloudless data points (mentioned in Section 3.4) with the AWS-measured counterparts. Figure A1 shows that the modeled and measured hourly $SR\downarrow_{cs}$ values agreed well ($R^2 = 0.99$), even though there is

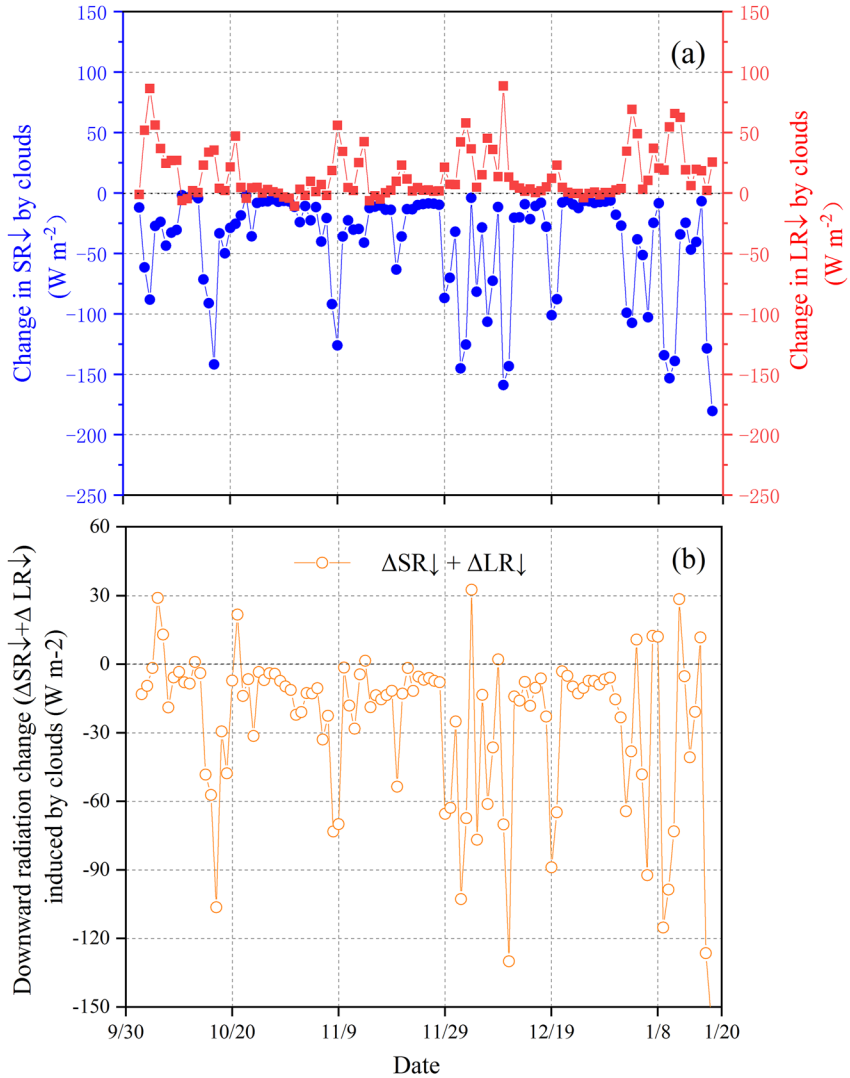

Figure A2. Downward radiations altered by clouds on the East Rongbuk glacier from October 2007 through January 2008.

a slight systematic model underestimation (9 W m^{-2} on average). Considering the local topography around our AWS (Figure 1), this underestimation might be caused by the additional reception of the SR↓ reflected from the snow-covered surroundings, which was captured by our AWS but could not be estimated by the SR↓$_{cs}$ model. Moreover, given the measurement accuracy (±5%) of the pyranometer (van den Broeke, van As, Reijmer, & van de Wal, 2004) and the AWS-measured SR↓ average (211 W m^{-2}), uncertainty in the AWS-measured SR↓ would be 11 W m^{-2} averagely, a value close to the model underestimation of 9 W m^{-2} mentioned above. The downward radiations altered by clouds we calculated are shown in Figure A2.

Data Availability Statement

The East Rongbuk glacier data from the second glacier inventory dataset of China is available at (S Liu et al., 2012), and the ERA5 reanalysis data are available at (Muñoz Sabater, 2019). The DEM with a 30 m resolution is made by NASA/METI/AIST/Japan Spacesystems and U.S./Japan ASTER Science Team (2019). The raw hourly AWS data used in this study are archived by National Tibetan Plateau Data Center (TPDC)/Third Pole Environment Data Center and are available at https://data.tpdc.ac.cn/zh-hans/disallow/b7d3d300-0820-4edb-ab3c-6911b9f-bcf03 (https://doi.org/10.11888/Cryos.tpdc.300253).

Acknowledgments
We are grateful to all staff participating in "the rehearsal of the 2008 Olympic torch relay on Mt. Everest in 2007." We thank Yaohui Li, Wentao Du, Jizu Chen, Zhenguo Niu, and Rui Bai for their suggestions and helps in writing the original manuscript. Six anonymous reviewers are gratefully acknowledged for their instructive comments, which significantly improved our manuscript. This paper is jointly financially supported by The Second Tibetan Plateau Scientific Expedition and Research Program (STEP, 2019QZKK0106) and the National Natural Science Foundation of China (42271151 and U2142208).

References

Ambach, W. (1974). The influence of cloudiness on the net radiation balance of a snow surface with high albedo. *Journal of Glaciology*, *13*(67), 73–84. https://doi.org/10.3189/S0022143000023388

Andreas, E. L. (1987). A theory for the scalar roughness and the scalar transfer coefficients over snow and sea ice. *Boundary-Layer Meteorology*, *38*(1–2), 159–184. https://doi.org/10.1007/bf00121562

Annear, R. L., & Wells, S. A. (2007). A comparison of five models for estimating clear-sky solar radiation. *Water Resources Research*, *43*(10). https://doi.org/10.1029/2006wr005055

Augustine, J. A., & Hodges, G. B. (2021). Variability of surface radiation budget components over the U.S. from 1996 to 2019—Has brightening ceased? *Journal of Geophysical Research: Atmospheres*, *126*(7), e2020JD033590. https://doi.org/10.1029/2020JD033590

Barandun, M., Pohl, E., Naegeli, K., McNabb, R., Huss, M., Berthier, E., et al. (2021). Hot spots of glacier mass balance variability in central Asia. *Geophysical Research Letters*, *48*(11), e2020GL092084. https://doi.org/10.1029/2020GL092084

Beesley, J. A. (2000). Estimating the effect of clouds on the arctic surface energy budget. *Journal of Geophysical Research*, *105*(D8), 10103–10117. https://doi.org/10.1029/2000JD900043

Benn, D. I., & Owen, L. A. (1998). The role of the Indian summer monsoon and the mid-latitude westerlies in Himalayan glaciation: Review and speculative discussion. *Journal of the Geological Society*, *155*(2), 353–363. https://doi.org/10.1144/gsjgs.155.2.0353

Bhattacharya, A., Bolch, T., Mukherjee, K., King, O., Menounos, B., Kapitsa, V., et al. (2021). High Mountain Asian glacier response to climate revealed by multi-temporal satellite observations since the 1960s. *Nature Communications*, *12*(1), 4133. https://doi.org/10.1038/s41467-021-24180-y

Bird, R. E., & Hulstrom, R. L. (1981). *A Simplified clear sky model for direct and diffuse insolation on horizontal surfaces* (Technical Report SERI/TR-642-761). Solar Energy Research Institute.

Bolch, T., Kulkarni, A., Kääb, A., Huggel, C., Paul, F., Cogley, J., et al. (2012). The state and fate of Himalayan glaciers. *Science*, *336*(6079), 310–314. https://doi.org/10.1126/science.1215828

Brock, B. W., Mihalcea, C., Kirkbride, M. P., Diolaiuti, G., Cutler, M. E. J., & Smiraglia, C. (2010). Meteorology and surface energy fluxes in the 2005–2007 ablation seasons at the Miage debris-covered glacier, Mont Blanc Massif, Italian Alps. *Journal of Geophysical Research: Atmospheres*, *115*(D9), D09106. https://doi.org/10.1029/2009JD013224

Brock, B. W., Willis, I. C., & Sharp, M. J. (2006). Measurement and parameterization of aerodynamic roughness length variations at Haut Glacier d'Arolla, Switzerland. *Journal of Glaciology*, *52*(177), 281–297. https://doi.org/10.3189/172756506781828746

Brutsaert, W. (1975). On a derivable formula for long-wave radiation from clear skies. *Water Resources Research*, *11*(5), 742–744. https://doi.org/10.1029/WR011i005p00742

Bush, B. C., Valero, F. P. J., Simpson, A. S., & Bignone, L. (2000). Characterization of thermal effects in pyranometers: A data correction algorithm for improved measurement of surface insolation. *Journal of Atmospheric and Oceanic Technology*, *17*(2), 165–175. https://doi.org/10.1175/1520-0426(2000)017<0165:coteip>2.0.co;2

Chang, C.-P., & Chen, G. T.-J. (1995). Tropical circulations associated with southwest monsoon onset and westerly surges over the south China sea. *Monthly Weather Review*, *123*(11), 3254–3267. https://doi.org/10.1175/1520-0493(1995)123<3254:tcawsm>2.0.co;2

Chen, J., Qin, X., Kang, S., Du, W., Sun, W., & Liu, Y. (2018). Effects of clouds on surface melting of Laohugou glacier No. 12, Western Qilian Mountains, China. *Journal of Glaciology*, *64*(243), 89–99. https://doi.org/10.1017/jog.2017.82

Colbeck, S. C. (1983). Theory of metamorphism of dry snow. *Journal of Geophysical Research: Oceans*, *88*(C9), 5475–5482. https://doi.org/10.1029/JC088iC09p05475

Conway, J. P., Abermann, J., Andreassen, L. M., Azam, M. F., Cullen, N. J., Fitzpatrick, N., et al. (2022). Cloud forcing of surface energy balance from in situ measurements in diverse mountain glacier environments. *The Cryosphere*, *16*(8), 3331–3356. https://doi.org/10.5194/tc-16-3331-2022

Conway, J. P., Cullen, N. J., Spronken-Smith, R. A., & Fitzsimons, S. J. (2015). All-sky radiation over a glacier surface in the southern Alps of New Zealand: Characterizing cloud effects on incoming shortwave, longwave and net radiation. *International Journal of Climatology*, *35*(5), 699–713. https://doi.org/10.1002/joc.4014

Cuffey, K., & Paterson, W. S. B. (2010). *The Physics of Glaciers_4th Edition*. Academic Press.

Ding, M., Yang, D., van den Broeke, M. R., Allison, I., Xiao, C., Qin, D., & Huai, B. (2020). The surface energy balance at Panda 1 station, Princess Elizabeth Land: A typical katabatic wind region in east Antarctica. *Journal of Geophysical Research: Atmospheres*, *125*(3), e2019JD030378. https://doi.org/10.1029/2019jd030378

Domine, F., Lauzier, T., Cabanes, A., Legagneux, L., Kuhs, W., Techmer, K., & Heinrichs, T. (2003). Snow metamorphism as revealed by scanning electron microscopy. *Microscopy Research and Technique*, *62*(1), 33–48. https://doi.org/10.1002/jemt.10384

Duan, A., & Wu, G. (2006). Change of cloud amount and the climate warming on the Tibetan Plateau. *Geophysical Research Letters*, *33*(22), L22704. https://doi.org/10.1029/2006GL027946

Duguay, C. R. (1993). *Radiation modeling in mountainous terrain: review and status*, In Mountain Research and Development (p. 339). https://doi.org/10.2307/3673761

Dyer, A. J. (1974). A review of flux-profile relationships. *Boundary-Layer Meteorology*, *7*(3), 363–372. https://doi.org/10.1007/BF00240838

Ebner, P. P., Schneebeli, M., & Steinfeld, A. (2015). Tomography-based monitoring of isothermal snow metamorphism under advective conditions. *The Cryosphere*, *9*(4), 1363–1371. https://doi.org/10.5194/tc-9-1363-2015

Favier, V., Wagnon, P., Chazarin, J.-P., Maisincho, L., & Coudrain, A. (2004). One-year measurements of surface heat budget on the ablation zone of Antizana Glacier 15, Ecuadorian Andes. *Journal of Geophysical Research*, *109*(D18), D18105. https://doi.org/10.1029/2003jd004359

Fugger, S., Fyffe, C. L., Fatichi, S., Miles, E., McCarthy, M., Shaw, T. E., et al. (2021). Understanding monsoon controls on the energy and mass balance of Himalayan glaciers. *The Cryosphere Discussions*, *2021*, 1–46. https://doi.org/10.5194/tc-2021-97

Fugger, S., Fyffe, C. L., Fatichi, S., Miles, E., McCarthy, M., Shaw, T. E., et al. (2022). Understanding monsoon controls on the energy and mass balance of glaciers in the Central and Eastern Himalaya. *The Cryosphere*, *16*(5), 1631–1652. https://doi.org/10.5194/tc-16-1631-2022

Giesen, R., Van den Broeke, M., Oerlemans, J., & Andreassen, L. (2008). Surface energy balance in the ablation zone of Midtdalsbreen, a glacier in southern Norway: Interannual variability and the effect of clouds. *Journal of Geophysical Research: Atmospheres (1984–2012)*, *113*(D21), 113. https://doi.org/10.1029/2008jd010390

Grenfell, T., Perovich, D., & Ogren, J. (1981). Spectral albedos of an alpine snowpack. *Cold Regions Science and Technology*, *4*(2), 121–127. https://doi.org/10.1016/0165-232X(81)90016-1

Greuell, W., & Konzelmann, T. (1994). Numerical modelling of the energy balance and the englacial temperature of the Greenland Ice Sheet. Calculations for the ETH-Camp location (West Greenland, 1155 m a.s.l.). *Global and Planetary Change*, *9*(1), 91–114. https://doi.org/10.1016/0921-8181(94)90010-8

Gubler, S., Gruber, S., & Purves, R. S. (2012). Uncertainties of parameterized surface downward clear-sky shortwave and all-sky longwave radiation. *Atmospheric Chemistry and Physics*, *12*(11), 5077–5098. https://doi.org/10.5194/acp-12-5077-2012

Guo, W., Liu, S., Xu, J., Wu, L., Shangguan, D., Yao, X., et al. (2015). The second Chinese glacier inventory: Data, methods and results. *Journal of Glaciology*, *61*(226), 357–372. https://doi.org/10.3189/2015JoG14J209

Hansen, A. C., & Foslien, W. E. (2015). A macroscale mixture theory analysis of deposition and sublimation rates during heat and mass transfer in dry snow. *The Cryosphere*, *9*(5), 1857–1878. https://doi.org/10.5194/tc-9-1857-2015

Holtslag, A. A. M., & De Bruin, H. A. R. (1988). Applied modeling of the nighttime surface energy balance over land. *Journal of Applied Meteorology*, *27*(1988), 689–704. https://doi.org/10.1175/1520-0450(1988)027<0689:amotns>2.0.co;2

Hugonnet, R., McNabb, R., Berthier, E., Menounos, B., Nuth, C., Girod, L., et al. (2021). Accelerated global glacier mass loss in the early twenty-first century. *Nature*, *592*(7856), 726–731. https://doi.org/10.1038/s41586-021-03436-z

Intrieri, J. M. (2002). An annual cycle of Arctic surface cloud forcing at SHEBA. *Journal of Geophysical Research*, *107*(C10), 8039. https://doi.org/10.1029/2000jc000439

Ji, Q., & Tsay, S.-C. (2009). A novel nonintrusive method to resolve the thermal dome effect of pyranometers: Instrumentation and observational basis. *Journal of Geophysical Research: Atmospheres*, *115*(D7), D00K21. https://doi.org/10.1029/2009JD013483

Ji, Q., Tsay, S.-C., Lau, K. M., Hansell, R. A., Butler, J. J., & Cooper, J. W. (2011). A novel nonintrusive method to resolve the thermal dome effect of pyranometers: Radiometric calibration and implications. *Journal of Geophysical Research: Atmospheres*, *116*(D24). https://doi.org/10.1029/2011JD016466

Jouberton, A., Shaw, T. E., Miles, E., McCarthy, M., Fugger, S., Ren, S., et al. (2022). Warming-induced monsoon precipitation phase change intensifies glacier mass loss in the southeastern Tibetan Plateau. *Proceedings of the National Academy of Sciences*, *119*(37), e2109796119. https://doi.org/10.1073/pnas.2109796119

Juszak, I., & Pellicciotti, F. (2013). A comparison of parameterizations of incoming longwave radiation over melting glaciers: Model robustness and seasonal variability. *Journal of Geophysical Research: Atmospheres*, *118*(8), 3066–3084. https://doi.org/10.1002/jgrd.50277

Kang, S., Zhang, Y., Chen, P., Guo, J., Zhang, Q., Cong, Z., et al. (2022). Black carbon and organic carbon dataset over the third pole. *Earth System Science Data*, *14*(2), 683–707. https://doi.org/10.5194/essd-14-683-2022

Kaser, G., Großhauser, M., & Marzeion, B. (2010). Contribution potential of glaciers to water availability in different climate regimes. *Proceedings of the National Academy of Sciences*, *107*(47), 20223–20227. https://doi.org/10.1073/pnas.1008162107

Kondo, J., & Yamazawa, H. (1986). Measurement of snow surface emissivity. *Boundary-Layer Meteorology*, *34*(4), 415–416. https://doi.org/10.1007/BF00120992

Kotlyakov, V. M., Zichu, X., Khromova, T. E., Zverkova, N. M., & Chernova, L. P. (2012). Contemporary glacier systems of continental Eurasia. *Doklady Earth Sciences*, *446*(1), 1095–1098. https://doi.org/10.1134/S1028334X12090036

Kuipers Munneke, P., van den Broeke, M. R., King, J. C., Gray, T., & Reijmer, C. H. (2012). Near-surface climate and surface energy budget of Larsen C ice shelf, Antarctic Peninsula. *The Cryosphere*, *6*(2), 353–363. https://doi.org/10.5194/tc-6-353-2012

Kuipers Munneke, P., van den Broeke, M. R., Reijmer, C. H., Helsen, M. M., Boot, W., Schneebeli, M., & Steffen, K. (2009). The role of radiation penetration in the energy budget of the snowpack at Summit, Greenland. *The Cryosphere*, *3*(2), 155–165. https://doi.org/10.5194/tc-3-155-2009

Lai, Y., Chen, X., Ma, Y., Chen, D., & Zhaxi, S. (2021). Impacts of the westerlies on planetary boundary layer growth over a valley on the north side of the central Himalayas. *Journal of Geophysical Research: Atmospheres*, *126*(3), e2020JD033928. https://doi.org/10.1029/2020JD033928

Lang, T., & Barros, A. (2004). Winter storms in the Central Himalayas. *Journal of the Meteorological Society of Japan*, *82*(3), 829–844. https://doi.org/10.2151/jmsj.2004.829

Le Toumelin, L., Amory, C., Favier, V., Kittel, C., Hofer, S., Fettweis, X., et al. (2021). Sensitivity of the surface energy budget to drifting snow as simulated by MAR in coastal Adelie Land, Antarctica. *The Cryosphere*, *15*(8), 3595–3614. https://doi.org/10.5194/tc-15-3595-2021

Liang, L., Cuo, L., & Liu, Q. (2019). Mass balance variation and associative climate drivers for the Dongkemadi glacier in the central Tibetan Plateau. *Journal of Geophysical Research: Atmospheres*, *124*(20), 10814–10825. https://doi.org/10.1029/2019JD030615

Liang, L., Cuo, L., & Liu, Q. (2020). Long-term temporal scale-dependent warming effects on the mass balance in the Dongkemadi glacier, Tibetan Plateau. *Journal of Geophysical Research: Atmospheres*, *125*(20), e2020JD033105. https://doi.org/10.1029/2020JD033105

Lindberg, F. (2005). Towards the use of local governmental 3-D data within urban climatology studies. *Mapping Image Science*, *2*, 32–37.

Li, L., Shen, H.-Y., Liu, C.-H., & Xiao, R.-X. (2020). Response of water level fluctuation to climate warming and wetting scenarios and its mechanism on Qinghai lake. *Climate Change Research*, *16*(5), 600–608. https://doi.org/10.12006/j.issn.1673-1719.2019.243

Li, S., Yao, T., Yang, W., Yu, W., & Zhu, M. (2018). glacier energy and mass balance in the inland Tibetan Plateau: Seasonal and interannual variability in relation to atmospheric changes. *Journal of Geophysical Research: Atmospheres*, *123*(12), 6390–6409. https://doi.org/10.1029/2017JD028120

Litt, M., Shea, J., Wagnon, P., Steiner, J., Koch, I., Stigter, E., & Immerzeel, W. (2019). Glacier ablation and temperature indexed melt models in the Nepalese Himalaya. *Scientific Reports*, *9*(1), 5264. https://doi.org/10.1038/s41598-019-41657-5

Liu, S., Guo, W., & Xu, J. (2012). The second glacier inventory dataset of China (version 1.0) (2006-2011) [Dataset]. National Tibetan Plateau Data Center/Third Pole Environment Data Center. https://doi.org/10.3972/glacier.001.2013.db

Liu, W., Ren, J., Qin, X., Liu, J., Liu, Q., Cui, X., & Wang, Y. (2010). Hydrological characteristics of the Rongbuk Glacier catchment in Mt. Qomolangma region in the central Himalayas, China. *Journal of Mountain Science*, *7*(2), 146–156. https://doi.org/10.1007/s11629-010-1069-4

Liu, W., Zhang, D., Qin, X., van den Broeke, M. R., Jiang, Y., Yang, D., & Ding, M. (2021). Monsoon clouds control the summer surface energy balance on East Rongbuk glacier (6,523 m above sea level), the northern of Mt. Qomolangma (everest). *Journal of Geophysical Research: Atmospheres*, *126*(8), e2020JD033998. https://doi.org/10.1029/2020JD033998

Mandal, A., Angchuk, T., Azam, M. F., Ramanathan, A., Wagnon, P., Soheb, M., & Singh, C. (2022). An 11-year record of wintertime snow-surface energy balance and sublimation at 4863 m a.s.l. on the Chhota Shigri Glacier moraine (Western Himalaya, India). *The Cryosphere*, *16*(9), 3775–3799. https://doi.org/10.5194/tc-16-3775-2022

Matthews, T., Perry, L. B., Koch, I., Aryal, D., Khadka, A., Shrestha, D., et al. (2020). Going to extremes: Installing the world's highest weather stations on Mount Everest. *Bulletin of the American Meteorological Society*, *101*(11), E1870–E1890. https://doi.org/10.1175/bams-d-19-0198.1

Meng, F., Su, F., Li, Y., & Tong, K. (2019). Changes in terrestrial water storage during 2003–2014 and possible causes in Tibetan Plateau. *Journal of Geophysical Research: Atmospheres*, *124*(6), 2909–2931. https://doi.org/10.1029/2018JD029552

Mi, D., & Xie, Z. (2002). *Glacier inventory of China: XI - The Ganga drainge basin and XII - Indus river drainge basin. Xian: Xi'an Cartographic* Publishing House.

Michel, D., Philipona, R., Ruckstuhl, C., Vogt, R., & Vuilleumier, L. (2008). Performance and uncertainty of CNR1 net radiometers during a one-year field comparison. *Journal of Atmospheric and Oceanic Technology*, *25*(3), 442–451. https://doi.org/10.1175/2007jtecha973.1

Mölg, T., Cullen, N. J., & Kaser, G. (2009). Solar radiation, cloudiness and longwave radiation over low-latitude glaciers: Implications for mass-balance modelling. *Journal of Glaciology*, *55*(190), 292–302. https://doi.org/10.3189/002214309788608822

Muñoz Sabater, J. (2019). ERA5-Land hourly data from 1981 to present [Dataset]. Copernicus Climate Change Service (C3S) Climate Data Store (CDS). Retrieved from https://cds.climate.copernicus.eu/cdsapp#!/dataset/reanalysis-era5-land?tab=overview

NASA/METI/AIST/Japan Spacesystems and U.S./Japan ASTER Science Team. (2019). ASTER Global Digital Elevation Model V003 [Dataset]. https://doi.org/10.5067/ASTER/ASTGTM.003

Oke, T. R. (1987). *Boundary layer climates* (2nd ed., p. 435). Routledge.

Pang, H., Hou, S., Zhang, W., Wu, S., Jenk, T. M., Schwikowski, M., & Jouzel, J. (2020). Temperature trends in the northwestern Tibetan Plateau constrained by ice core water isotopes over the past 7,000 years. *Journal of Geophysical Research: Atmospheres*, *125*(19), e2020JD032560. https://doi.org/10.1029/2020JD032560

Pellicciotti, F., Raschle, T., Huerlimann, T., Carenzo, M., & Burlando, P. (2011). Transmission of solar radiation through clouds on melting glaciers: A comparison of parameterizations and their impact on melt modelling. *Journal of Glaciology*, *57*(202), 367–381. https://doi.org/10.3189/002214311796406013

Philipona, R. (2002). Underestimation of solar global and diffuse radiation measured at Earth's surface. *Journal of Geophysical Research:Atmospheres*, *107*(D22), 4654. ACL 15-11-ACL 15-18. https://doi.org/10.1029/2002JD002396

Potocki, M., Mayewski, P. A., Matthews, T., Perry, L. B., Schwikowski, M., Tait, A. M., et al. (2022). Mt. Everest's highest glacier is a sentinel for accelerating ice loss. *NPJ Climate and Atmospheric Science*, *5*(1), 7. https://doi.org/10.1038/s41612-022-00230-0

Prata, F. (1996). A new long-wave formula for estimating downward clear-sky radiation at the surface. *Quarterly Journal of the Royal Meteorological Society*, *122*(533), 1127–1151. https://doi.org/10.1002/qj.49712253306

Pritchard, H. D. (2019). Asia's shrinking glaciers protect large populations from drought stress. *Nature*, *569*(7758), 649–654. https://doi.org/10.1038/s41586-019-1240-1

Qiu, J. (2008). China: The third pole. *Nature*, *454*(7203), 393–396. https://doi.org/10.1038/454393a

Ramanathan, V., Cess, R. D., Harrison, E. F., Minnis, P., Barkstrom, B. R., Ahmad, E., & Hartmann, D. (1989). Cloud-radiative forcing and climate: Results from the Earth radiation budget experiment. *Science*, *243*(4887), 57–63. https://doi.org/10.1126/science.243.4887.57

Ren, J., Qin, D., kang, S., Hou, S., Pu, J., & Jing, Z. (2004). Glacier variations and climate warming and drying in the central Himalayas. *Chinese Science Bulletin*, *49*(1), 65. https://doi.org/10.1360/03wd0148

Rodrigo, J., Buchlin, J.-M., Beeck, J., Lenaerts, J., & Van den Broeke, M. (2012). Evaluation of the Antarctic surface wind climate from ERA reanalyses and RACMO2/ANT simulations based on automatic weather stations. *Climate Dynamics*, *40*(1–2), 353–376. https://doi.org/10.1007/s00382-012-1396-y

Ruckstuhl, C., Philipona, R., Morland, J., & Ohmura, A. (2007). Observed relationship between surface specific humidity, integrated water vapor, and longwave downward radiation at different altitudes. *Journal of Geophysical Research: Atmospheres*, *112*(D3), D03302. https://doi.org/10.1029/2006JD007850

Sanchez, G., Serrano, A., Cancillo, M. L., & Garcia, J. A. (2015). Pyranometer thermal offset: Measurement and analysis. *Journal of Atmospheric and Oceanic Technology*, *32*(2), 234–246. https://doi.org/10.1175/jtech-d-14-00082.1

Scherler, D., Bookhagen, B., & Strecker, M. R. (2011). Spatially variable response of Himalayan glaciers to climate change affected by debris cover. *Nature Geoscience*, *4*(3), 156–159. https://doi.org/10.1038/ngeo1068

Shean, D. E., Bhushan, S., Montesano, P., Rounce, D. R., Arendt, A., & Osmanoglu, B. (2020). A systematic, regional assessment of high mountain Asia glacier mass balance. *Frontiers of Earth Science*, *7*. https://doi.org/10.3389/feart.2019.00363

Sicart, J. E., Hock, R., Ribstein, P., & Chazarin, J. P. (2010). Sky longwave radiation on tropical Andean glaciers: Parameterization and sensitivity to atmospheric variables. *Journal of Glaciology*, *56*(199), 854–860. https://doi.org/10.3189/002214310794457182

Sicart, J. E., Hock, R., & Six, D. (2008). Glacier melt, air temperature, and energy balance in different climates: The Bolivian Tropics, the French Alps, and northern Sweden. *Journal of Geophysical Research*, *113*(D24), D24113. https://doi.org/10.1029/2008jd010406

Sicart, J. E., Wagnon, P., & Ribstein, P. (2005). Atmospheric controls of the heat balance of Zongo Glacier (16°S, Bolivia). *Journal of Geophysical Research*, *110*(D12), D12106. https://doi.org/10.1029/2004jd005732

Stigter, E. E., Litt, M., Steiner, J. F., Bonekamp, P. N. J., Shea, J. M., Bierkens, M. F. P., & Immerzeel, W. W. (2018). The importance of snow sublimation on a Himalayan glacier. *Frontiers of Earth Science*, *6*(108). https://doi.org/10.3389/feart.2018.00108

Stigter, E. E., Steiner, J. F., Koch, I., Saloranta, T. M., Kirkham, J. D., & Immerzeel, W. W. (2021). Energy and mass balance dynamics of the seasonal snowpack at two high-altitude sites in the Himalaya. *Cold Regions Science and Technology*, *183*, 103233. https://doi.org/10.1016/j.coldregions.2021.103233

Sun, W., Qin, X., Wang, Y., Chen, J., Du, W., Zhang, T., & Huai, B. (2018). The response of surface mass and energy balance of a continental glacier to climate variability, Western Qilian Mountains, China. *Climate Dynamics*, *50*(9–10), 3557–3570. https://doi.org/10.1007/s00382-017-3823-6

Van den Broeke, M. R., & Lipzig, N. (2003). Factors controlling the near-surface wind field in Antarctica. *Monthly Weather Review*, *131*(4), 733–743. https://doi.org/10.1175/1520-0493(2003)131<0733:FCTNSW>2.0.CO;2

Van den Broeke, M. R., Reijmer, C., Van As, D., & Boot, W. (2006). Daily cycle of the surface energy balance in Antarctica and the influence of clouds. *International Journal of Climatology*, *26*(12), 1587–1605. https://doi.org/10.1002/joc.1323

Van Den Broeke, M. R., Reijmer, C., Van As, D., Van de Wal, R., & Oerlemans, J. (2005). Seasonal cycles of Antarctic surface energy balance from automatic weather stations. *Annals of Glaciology*, *41*, 131–139. https://doi.org/10.3189/172756405781813168

van den Broeke, M. R., Reijmer, C. H., & van de Wal, R. S. W. (2004). A study of the surface mass balance in Dronning Maud Land, Antarctica, using automatic weather stations. *Journal of Glaciology*, *50*(171), 565–582. https://doi.org/10.3189/172756504781829756

van den Broeke, M. R., Reijmer, C., & van de Wal, R. S. (2004). Surface radiation balance in Antarctica as measured with automatic weather stations. *Journal of Geophysical Research*, *109*(D9), D09103. https://doi.org/10.1029/2003jd004394

van den Broeke, M. R., Smeets, P., & Ettema, J. (2008). Surface layer climate and turbulent exchange in the ablation zone of the west Greenland ice sheet. *International Journal of Climatology*, *29*(15), 2309–2323. https://doi.org/10.1002/joc.1815

van den Broeke, M. R., Smeets, P., Ettema, J., & Munneke, P. K. (2008). Surface radiation balance in the ablation zone of the west Greenland ice sheet. *Journal of Geophysical Research*, *113*(D13), D13105. https://doi.org/10.1029/2007jd009283

van den Broeke, M. R., Smeets, P., Ettema, J., van der Veen, C., van de Wal, R., & Oerlemans, J. (2008). Partitioning of melt energy and meltwater fluxes in the ablation zone of the west Greenland ice sheet. *The Cryosphere*, *2*(2), 179–189. https://doi.org/10.5194/tc-2-179-2008

van den Broeke, M. R., Smeets, C. J. P. P., & van de Wal, R. S. W. (2011). The seasonal cycle and interannual variability of surface energy balance and melt in the ablation zone of the west Greenland ice sheet. *The Cryosphere*, *5*(2), 377–390. https://doi.org/10.5194/tc-5-377-2011

van den Broeke, M. R., van As, D., Reijmer, C., & van de Wal, R. (2004c). Assessing and improving the quality of unattended radiation observations in Antarctica. *Journal of Atmospheric and Oceanic Technology*, *21*(9), 1417–1431. https://doi.org/10.1175/1520-0426(2004)021<1417:aaitqo>2.0.co;2

Veldhuijsen, S. B. M., de Kok, R. J., Stigter, E. E., Steiner, J. F., Saloranta, T. M., & Immerzeel, W. W. (2021). Spatial and temporal patterns of snowmelt refreezing in a Himalayan catchment. *Journal of Glaciology*, *68*(268), 1–21. https://doi.org/10.1017/jog.2021.101

Wagnon, P., Sicart, J.-E., Berthier, E., & Chazarin, J.-P. (2003). Wintertime high-altitude surface energy balance of a Bolivian glacier, Illimani, 6340 m above sea level. *Journal of Geophysical Research*, *108*(D6). https://doi.org/10.1029/2002jd002088

Wang, B. (2006). *The Asian monsoon*. Springer Praxis.

Wang, W., Zender, C. S., & van As, D. (2018). Temporal characteristics of cloud radiative effects on the Greenland ice sheet: Discoveries from multiyear automatic weather station measurements. *Journal of Geophysical Research: Atmospheres*, *123*(20), 11348–311361. https://doi.org/10.1029/2018JD028540

Webster, P. J., & Yang, S. (2010). Monsoon and Enso: Selectively interactive systems. *Quarterly Journal of the Royal Meteorological Society*, *118*(507), 877–926. https://doi.org/10.1002/qj.49711850705

Wu, G., Duan, A., Liu, Y., Mao, J., Ren, R., Bao, Q., et al. (2015). Tibetan Plateau climate dynamics: Recent research progress and outlook. *National Science Review*, *2*(1), 100–116. https://doi.org/10.1093/nsr/nwu045

Xu, B., Cao, J., Hansen, J., Yao, T., Joswia, D. R., Wang, N., et al. (2009). Black soot and the survival of Tibetan glaciers. *Proceedings of the National Academy of Sciences*, *106*(52), 22114–22118. https://doi.org/10.1073/pnas.0910444106

Yang, D., Ding, M., Dou, T., Han, W., Liu, W., Zhang, J., et al. (2021). On the differences in precipitation type between the Arctic, Antarctica and Tibetan Plateau. *Frontiers of Earth Science*, *9*(19). https://doi.org/10.3389/feart.2021.607487

Yang, W., Guo, X., Yao, T., Yang, K., Zhao, L., Li, S., & Zhu, M. (2011). Summertime surface energy budget and ablation modeling in the ablation zone of a maritime Tibetan glacier. *Journal of Geophysical Research: Atmospheres*, *116*(D14), D14116. https://doi.org/10.1029/2010jd015183

Yang, W., Yao, T., Guo, X., Zhu, M., Li, S., & Kattel, D. B. (2013). Mass balance of a maritime glacier on the southeast Tibetan Plateau and its climatic sensitivity. *Journal of Geophysical Research: Atmospheres*, *118*(17), 9579–9594. https://doi.org/10.1002/jgrd.50760

Yang, W., Yao, T., Zhu, M., & Wang, Y. (2017). Comparison of the meteorology and surface energy fluxes of debris-free and debris-covered glaciers in the southeastern Tibetan Plateau. *Journal of Glaciology*, *63*(242), 1090–1104. https://doi.org/10.1017/jog.2017.77

Yang, X., Zhang, T., Qin, D., Kang, S., & Qin, X. (2018). Characteristics and changes in air temperature and glacier's response on the north slope of Mt. Qomolangma (Mt. Everest). *Arctic Antarctic, and Alpine Research*, *43*(1), 147–160. https://doi.org/10.1657/1938-4246-43.1.147

Yang, X., Zhang, T., Qin, D., Qin, X., & Yang, Y. (2015). Observational study of surface wind regime on the north slope of mount Qomolangma (Mount Everest). *Arctic Antarctic, and Alpine Research*, *47*(4), 807–817. https://doi.org/10.1657/aaar00c-13-132

Yao, T., Thompson, L., Yang, W., Yu, W., Gao, Y., Guo, X., et al. (2012). Different glacier status with atmospheric circulations in Tibetan Plateau and surroundings. *Nature Climate Change*, *2*(9), 663–667. https://doi.org/10.1038/nclimate1580

Ye, Q., Bolch, T., Naruse, R., Wang, Y., Zong, J., Wang, Z., et al. (2015). Glacier mass changes in Rongbuk catchment on Mt. Qomolangma from 1974 to 2006 based on topographic maps and ALOS PRISM data. *Journal of Hydrology*, *530*, 273–280. https://doi.org/10.1016/j.jhydrol.2015.09.014

Zhang, G., Kang, S., Fujita, K., Huintjes, E., Xu, J., Yamazaki, T., et al. (2013). Energy and mass balance of Zhadang glacier surface, central Tibetan Plateau. *Journal of Glaciology*, *59*(213), 137–148. https://doi.org/10.3189/2013JoG12J152

Zhang, T., Bowling, S. A., & Stamnes, K. (1997). Impact of the atmosphere on surface radiative fluxes and snowmelt in the Arctic and Subarctic. *Journal of Geophysical Research*, *102*(D4), 4287–4302. https://doi.org/10.1029/96JD02548

Zhang, T., Stamnes, K., & Bowling, S. A. (1996). Impact of clouds on surface radiative fluxes and snowmelt in the Arctic and Subarctic. *Journal of Climate*, *9*(9), 2110–2123. https://doi.org/10.1175/1520-0442(1996)009<2110:iocosr>2.0.co;2

Zhou, L., Zou, H., Ma, S., & Li, P. (2008). Study on impact of the South Asian summer monsoon on the down-valley wind on the northern slope of Mt. Everest. *Geophysical Research Letters*, *35*(14), L14811. https://doi.org/10.1029/2008GL034151

Zhu, M., Yao, T., Yang, W., Maussion, F., Huintjes, E., & Li, S. (2015). Energy- and mass-balance comparison between Zhadang and Parlung No. 4 glaciers on the Tibetan plateau. *Journal of Glaciology*, *61*(227), 595–607. https://doi.org/10.3189/2015JoG14J206

Zhu, M., Yao, T., Yang, W., Xu, B., & Wang, X. (2016). Evaluation of parameterizations of incoming longwave radiation in the high-mountain region of the Tibetan plateau. *Journal of Applied Meteorology and Climatology*, *56*(4), 833–848. https://doi.org/10.1175/JAMC-D-16-0189.1

Zhu, M., Yao, T., Yang, W., Xu, B., Wu, G., & Wang, X. (2018). Differences in mass balance behavior for three glaciers from different climatic regions on the Tibetan Plateau. *Climate Dynamics*, *50*(9), 3457–3484. https://doi.org/10.1007/s00382-017-3817-4

Zou, H. (1996). Seasonal variation and trends of TOMS ozone over Tibet. *Geophysical Research Letters*, *23*(9), 1029–1032. https://doi.org/10.1029/96GL00767

Zou, H., Ma, S., Zhou, L., Li, P., & Li, A. (2009). Measured turbulent heat transfer on the northern slope of Mt. Everest and its relation to the south Asian summer monsoon. *Geophysical Research Letters*, *36*(9), L09810. https://doi.org/10.1029/2008gl036984

Zou, H., Zhou, L., Ma, S., Li, P., Wang, W., Li, A., et al. (2008). Local wind system in the Rongbuk valley on the northern slope of Mt. Everest. *Geophysical Research Letters*, *35*(13), L13813. https://doi.org/10.1029/2008gl033466